

A mountain ridge model for quantifying oblique mountain wave propagation and distribution

Sebastian Rhode¹, Peter Preusse¹, Manfred Ern¹, Jörn Ungermann¹, Lukas Krasauskas¹, Julio Bacmeister², and Martin Riese¹

¹Institute of Energy and Climate Research, Stratosphere (IEK-7), Forschungszentrum Jülich, Jülich, Germany

²National Center for Atmospheric Research (NCAR), Boulder, CO, USA

Correspondence: Sebastian Rhode (s.rhode@fz-juelich.de)

Abstract.

Following the current understanding of gravity waves (GWs) and especially mountain waves (MWs), they have ~~high potential of a high potential for~~ horizontal propagation from their source. This horizontal propagation and therefore the transport of energy is usually not well represented in MW parameterizations of numerical weather prediction and general circulation models.

5 ~~The lack thereof possibly leads to shortcomings in the model's prediction as e.g. the cold pole bias in the Southern Hemisphere and the polar vortex breaking down too late.~~ In this study, we present a mountain wave model (MWM) for ~~quantification of the~~ the quantification of horizontal propagation of orographic gravity waves. This model determines MW source location ~~and associates their~~ from topography data and estimates MW parameters from a fit of idealized ~~Gaussian-shaped mountains to topography data~~ Gaussian-shaped mountains to the elevation. Propagation and refraction of these MWs in the atmosphere ~~is are~~

10 modeled using the ~~ray-tracer~~ ray tracer GROGRAT. Ray-tracing each MW individually allows for an estimation of momentum transport due to both vertical and horizontal propagation. The MWM is a capable tool for the analysis of MW propagation and global MW activity and can support the understanding of observations and improvement of MW parameterizations in GCMs. This study presents the ~~MWM-model~~ itself and gives validations of MW induced temperature perturbations to ECMWF IFS numerical weather prediction data and estimations of ~~GWMF-GW momentum flux (GWMF)~~

15 observations. The MWM is capable of reproducing the general features and amplitudes of both of these data sets and, in addition, is used to explain some observational features by investigating MW parameters along their trajectories.

1 Introduction

Gravity waves (GWs) are atmospheric waves for which gravity or buoyancy acts as the restoring force (Fritts, 1984). They are an important dynamical process and interact with the ~~large-scale flow~~ large-scale flow (e.g. Holton, 1983; Andrews et al., 1987)

20 and contribute to the generation of clouds (e.g. Thayer et al., 2003; Saha et al., 2020). Since they propagate ~~vertically~~ through the atmosphere, both vertically and horizontally, they transport momentum from the lower atmosphere, or even the ground, to higher levels such as the stratosphere, mesosphere, and lower thermosphere. This relocation of momentum is one of the drivers of the Brewer-Dobson-Circulation (BDC) and the main driver of the upper, mesospheric branch of the residual circulation (e.g.

McIntyre, 1998; Fritts and Alexander, 2003). Various studies also argue for a significant role of gravity waves in the occurrence
25 of Sudden Stratospheric Warming (SSW) events (e.g. Whiteway et al., 1997; Kidston et al., 2015) and even their shape, i.e. whether the polar vortex splits or displaces (Albers and Birner, 2014; Ern et al., 2016; Song et al., 2020).

In addition, the effects of GWs are a major uncertainty in climate ~~projection~~ projections and numerical weather ~~forecast~~ forecasts (Shepherd, 2014). On the one hand, GWs have a significant impact on the dynamics of the atmosphere and even ~~larger-seale~~ larger-scale climate phenomena, on the other hand, they have to be parameterized within general circulation models
30 (GCMs). While ~~larger-seale~~ larger-scale GWs are resolved by the models, ~~small-seale~~ small- and medium-scale GWs caused by the sub-grid-scale orography and convection are typically approximated by a parameterization scheme (e.g. Lott and Miller, 1997; Kim et al., 2003; Xie et al., 2020). Following (Skamarock, 2004), the shortest resolved scales are about 4 times the grid resolution, which translates to about 500 – 1000 km for long-term GCM simulations. Shorter GWs are considered small-scale in this study. One particular shortcoming of these parameterizations employed in GCMs is the commonly used column-wise
35 calculation approach, which does not allow for the GW's momentum to be transported horizontally, whereby the corresponding GW drag will be exerted above the mountains. However, a high potential of horizontal GW propagation has been found both in observations and model studies (e.g. Preusse et al., 2002; Sato et al., 2012; Krisch et al., 2017; Ehard et al., 2017; Strube et al., 2021).

~~Another shortcoming of current GCMs is poor performance in the Southern Hemisphere dynamics, leading to the polar
40 vortex breaking down too late in spring and too low temperatures above the South Pole (cold-pole bias) (Butchart et al., 2011). Studies have shown that introducing north-south hemispheric asymmetry in orographic GW drag tuning can alleviate this shortcoming significantly (Garcia et al., 2017). Enhancing the Southern Hemisphere GW drag by a factor of 2 over that in the Northern Hemisphere leads to much better agreement between the simulated dynamical and chemical structure of the Southern Hemisphere polar vortex and observations while optimizing the model's performance in the Northern Hemisphere. In a different
45 study, (Polichtchouk et al., 2018) show that a non-orographic GW parameterization with increased drag improves the models prediction of the polar vortex breakdown. A possible reason for the underestimation of gravity wave drag in the southern polar vortex (McLandress et al., 2012) is the missing representation of oblique GW propagation (Wu and Eckermann, 2008; Strube et al., 2021; Fritts and Alexander, 2013) and possibly the under-representation of small-scale Ocean Islands (Alexander et al., 2009, 2010; Garfinkel and Oman, 2018; Hindley et al., 2019). Both processes could play an important role in explaining the missing wave drag at 60°S in climate and chemistry models.~~

50 Although GWs can be excited by various processes, e.g. convection, jet imbalances, and even volcanic eruptions (Wright et al., 2022; Ern et al., 2022), one of the major and most predictable sources of gravity waves is wind flow over orography, by which air parcels are displaced vertically. These stationary (with respect to the ground) mountain waves (MWs) propagate through the atmosphere, both vertically and horizontally. In the middle atmosphere, they can be measured from satellites (e.g. Eckermann and Preusse, 1999; Preusse et al., 2002; Jiang et al., 2004; Eckermann and Wu, 2012). The strength of the excited
55 MWs depends on the height and shape of the orography, the velocity of the ~~low-level flow~~ low-level flow, and the propagation conditions due to the winds above. At ~~midlatitudes~~ mid-latitudes, westerly winds prevail in the troposphere and north-south oriented ridges are expected to be particularly effective MW sources. Accordingly, the Rocky Mountains and the Andes are regions in which particularly high MW activity is expected. Indeed, for both mountain chains severe clear air turbulence due to

mountain waves has caused major aviation incidents (e.g. Smithsonian Magazine, 2005; Boldmethod, 2016; Aviación Global, 60 2019). ~~However, climatologies-~~

~~Strong GW activity in the troposphere, however, does not always directly translate to high GW activity in the stratosphere, although these MWs should propagate upwards. Climatologies~~ of GWs for the mid-stratosphere show only moderate GW activity over both the Rocky ~~mountains~~ Mountains and the Andes north of 40°S (e.g. Geller et al., 2013; Ern et al., 2018; Hindley et al., 2020). Likewise, the highest mountains on Earth, the ~~Himalayas~~ Himalaya, have only moderate impact on middle 65 atmosphere GW distributions. In order to understand this comparatively low stratospheric GW activity, ~~the observations need to be combined with a model study focusing on mountain waves~~ observations might be aided by model studies focusing on specific types of GWs. A model describing orographic GW propagation from source to breaking, for example, could shed light on the orographic part of the measured GW spectrum and help disentangle it from other sources. The combination of model and observation data enriches the analysis by providing more data to base the conclusions on but does also provide an opportunity 70 to probe the underlying theory in a real-world application.

In this study, we present a mountain wave model (MWM) capable of estimating the sources of orographic gravity waves similar to the approach by Bacmeister (1993) and Bacmeister et al. (1994). The propagation of the so-determined MWs throughout the atmosphere is modeled using the ray-tracer GROGRAT (Marks and Eckermann, 1995). Refraction of GWs due to horizontal gradients and time dependence of the background fields is considered within the ray-tracer. Results include 4-dimensional 75 momentum flux distributions, drag exerted on the background winds, and estimations of the residual temperature perturbations caused by the MWs. Compared to previous studies, we aim for ~~a~~ a higher accuracy in terms of mountain source detection by a fit of an idealized mountain shape at arbitrary angles. Additionally, we are considering wind-flow blocking and surface friction effects in the ~~low-level~~ low-level winds to improve modeled MW amplitudes and field characteristics. We are validating our model against satellite and model data to a higher degree of detail and emphasis on the MWM than in previous studies (e.g. 80 Jiang et al., 2002, 2004). For this, we consider data at altitudes of 15-25 km, which is low enough for a comparison of the effect of primary MWs before and after wind filtering in the atmosphere. Satellite data at these low altitudes have not been used for such a comparison before.

The described MWM is used to explain GW features in satellite data by investigating their wave characteristics from source to observation altitude. MW propagation patterns throughout the year are predicted and agree ~~to~~ with previous studies of 85 oblique MW spread. Therefore this model might be used for identifying MW propagation ~~pattern~~ patterns in further studies for improving MW parameterizations in GCMs by approximating their horizontal spread.

This article is organized as follows: First, Sect. 2 introduces the data used in this study. A general description of the mountain wave model is given in Sect. 3, which describes the detection of mountain wave sources, estimation of launch parameters, and modeling of the propagation. In addition, the post-processing of MWM data resulting in reconstructions of residual temperature 90 and gravity wave momentum flux (GWMF) distributions is discussed. Following this, a brief validation of the model is given in Sect. 4 including an investigation of the detected scales and a comparison to ECMWF operational analysis temperature data. In Sect. 5 the model's capability to predict horizontal GW propagation is shown by comparison with HIRDLS satellite data. ~~Predicted GW parameters~~ Calculated GW parameters along the ray paths and their change ~~through the observation altitudes~~

~~an-wind-blocking-with altitude and critical level filtering~~ are considered as possible causes of some observational features. In addition, predictions of horizontal GWMF ~~pattern-patterns~~ throughout the year are shown, which give first insight ~~in-into~~ the universality of horizontal propagation. Finally, the results are summarized in Sect. 6 and concluding remarks are given.

2 Data

This study uses ~~topography data-the ETOPO1 topography data (Amante and Eakins, 2009)~~ for the ridge finding ~~as well as~~ atmospheric background winds and temperature ~~from ERA5 reanalysis (Hersbach et al., 2020)~~ for MW propagation ~~modelling-~~ ~~Satellite modeling via ray-tracing. HIRDLS satellite~~ observations of gravity wave momentum fluxes (GWMFs) are used for a validation and comparison. The used data sets are presented in the following sections.

2.1 Topography data

The underlying topographic elevation data used in this study is taken from the ETOPO1 GLOBAL RELIEF MODEL (Amante and Eakins, 2009; Center, 2009) data set. This data is available in two versions: one describes the bedrock elevation only, ~~and~~ the other considers also the ice surface, i.e. glaciers and ice sheets. Since we are interested in the elevation encountered by the ~~low-level-low-level~~ flow, we use the data including the ice surface. This data set models the earth's surface, including ocean bathymetry, on ~~an-a resolution of 1 arc-minute-resolution-, or about 1.85 km at the equator,~~ and is combined from multiple global and regional data sets. However, we set all regions below sea level, which are not relevant for our analysis, to zero to approximate an ocean surface.

2.2 Atmospheric backgrounds

The atmospheric background wind and temperature data used for ray-tracing of MWs are generated from ECMWF ERA5 reanalysis data (Hersbach et al., 2020; C3S, 2017), sampled on a $0.3^\circ \times 0.3^\circ$ grid, ~~or about 33 km \times 33 km at the equator.~~ For our ray-tracing experiments, we want the background to contain all global and synoptic scale features but no GWs, which are potentially resolved by the numerical weather prediction (NWP) model. Following Strube et al. (2020), a scale separation approach is therefore applied to the data set using a zonal Fourier transform with a cutoff zonal ~~wave-number-of-18-~~ ~~wavenumber of 18, which correspond to wavelengths of about 2200 km at the equator.~~ In the meridional direction, the data is smoothed using a 3rd order Savitzky-Golay filter of 31 subsequent data points ($\sim 9^\circ$ total window width). For the use in GROGRAT, the smoothed background is sampled onto a grid of 2° latitude and 2.5° longitude, ~~or about 220 km and 280 km at the equator.~~ In the vertical the data is interpolated to equidistant altitudes of 0.5 km spacing. ~~For global ray-tracing experiments, 6 hourly snapshots, and for the specific case study of the Southern Andes in Sec. 4.2, hourly snapshots are used. To ensure smooth transitions in between, GROGRAT uses a 4-dimensional spline interpolation.~~

~~In addition to the ERA5 reanalysis data, single snapshots of operational forecast data of the ECMWF integrated forecast system (IFS) is used for validation of MW temperature perturbations in Sec. 4.2. This data set is given on a higher resolution of 0.1° , or about 10 km, in the horizontal and allows therefore resolution of GWs down to about 40 km (Skamarock, 2004).~~

125 The scale separation is performed analogously to the ERA5 data described above (the number of points in the meridional filter has been increased to 91 to achieve the same filter width of $\sim 9^\circ$).

2.3 HIRDLS satellite data

The horizontal GWMF distributions generated by our MWM for the year 2006 are validated and compared in Sect. 5.1 to satellite data from the High Resolution Dynamics Limb Sounder (HIRDLS, Gille et al. (2003)) instrument. The horizontal
130 sampling of these measurements is about 80 – 100 km along track. Here we use a data set specially prepared for the UTLS region, spanning the altitudes from 14 km to 25 km. As discussed ~~in-by~~ Strube et al. (2020), below 20 km altitude zonal ~~wave-numbers wavenumbers~~ of 10 and higher need to be taken into account ~~in-order~~ to describe the background. These cannot be self-consistently estimated from a single-track low Earth orbit satellite (Salby and Callaghan, 1997). In order to isolate the ~~small-seale small-scale~~ gravity wave (GW) contributions, ERA5 background data with an altitude-dependent zonal ~~wave~~
135 ~~number wavenumber~~ cutoff has been subtracted from the retrieved HIRDLS temperature measurements. Below 10 km altitude a cutoff at zonal ~~wave-number wavenumber~~ 20 (about 2000 km at the equator), above 20 km a cutoff at 6 (about 6700 km at the equator) has been used. In between, the cutoff decreases linearly from 20 to 6. In addition, the background removal as described in Ern et al. (2018) that is based on HIRDLS data only has been applied in a second step to account for imperfections of ERA5. The resulting vertical profiles of temperature residuals have been used for the calculation of GWMF as described in
140 Ern et al. (2018). ~~In-order-to~~ To analyze the lower stratosphere (20 km and below) and simultaneously avoid the influence of the tropopause, the vertical window of the MEM/HA method (Preusse et al., 2002) was reduced from 10 km, which is usually used for stratospheric altitudes (e.g. Ern et al., 2004), to 5 km. Such a reduced window size is adequate, since in the lower stratosphere the average vertical wavelengths are much lower than in the mid stratosphere and mesosphere (e.g. Chane-Ming et al., 2000; Yan et al., 2010; Ern et al., 2018). In addition, the HIRDLS data set has been high-pass filtered in terms of vertical
145 wavenumbers using a ~~5th-order 5th-order~~ Butterworth filter with vertical wavelength cutoff at 12 km, similar to Ehard et al. (2015).

For this paperstudy, GWMF is binned within rectangular overlapping bins of 15° in longitude and 5° in latitude sampled every 5° in longitude and 2.5° in latitude from the original profiles given along the satellite orbits. The vertical resolution of the data set is 1 km, which corresponds to the vertical resolution of HIRDLS. Note that due to the vertical window of 5 km
150 used in the MEM/HA method the given levels are representative for ± 2.5 km around the corresponding altitude.

3 Mountain Wave Model

The Mountain Wave Model (MWM) presented in this paper consists of three independent parts. The first one is the identification of mountain ridges from elevation data. The use of ridges follows the approach presented ~~in-by~~ Bacmeister (1993) and Bacmeister et al. (1994), but different methods are used for the parameter determination. The second part of the model consists
155 of the translation of the determined ridge parameters into MW launch parameters. In the third part, the so-initialized gravity waves are propagated through the background atmosphere using the ray-tracer GROGRAT (Marks and Eckermann, 1995).

Interval No.	lower boundary [km]	upper boundary [km]
1	80	150
2	150	250
3	250	400
4	400	600
5	600	850
6	850	1100
7	1100	1500
8	1500	2000

Table 1. Band-pass intervals used for detecting mountain ridges in the topography for this study.

3.1 Ridge Identification

The first specific task of our MWM is the estimation of MW parameters, such as horizontal wavelength, amplitude, orientation, and location from a fit of an idealized mountain ridge to the topography. This allows launching a monochromatic GW exerted by the detected mountain ridge later on. An overview of the algorithm and examples for the intermediate steps of the ridge identification as applied to a part of South America is given in Fig. 1.

First, the elevation data is divided into overlapping slices of 10° in latitude and every 7.5° width in latitude spanning the full globe in longitude. These slices are generated every 7.5° in latitude, leading to a 2.5° overlap, and interpolated onto an equidistant grid in terms of physical distance. This avoids possible errors in the fitted width and length of the ridges due to projection at high latitudes. Technically this limits the maximum ridge length to 10° in latitude, which in practice, however, never occurred. In order to identify mountain ridges of different scales, a Gaussian band-pass filter is applied as a second step. This also removes large scale is calculated as the difference between the elevation data convoluted with a 2-dimensional Gaussian function of different scales which are given as the limits of the considered scale interval. The filtering also removes large-scale plateaus, which are not of interest in this iteration of our model. In this study, we are using the band-pass intervals given in **table** Table 1. The resulting GW spectrum consists of both, inertia-gravity waves and non-hydrostatic GWs, with $\hat{\omega} \gg f$. In the following, both are referred to as GWs.

For each band-pass filtered slice of topography, the main ridge lines (or arêtes) are identified by detecting a corresponding sign change in the gradient, which itself is calculated by a-convolution with an optimized 3×3 Sobel operator (the Scharr operator, Jähne et al., 1999). To account for ridges of different orientations, this identification (and gradient calculation) is performed for 4 different directions separately (zonal, meridional, and both diagonals). The result of this step is a field of line structures, representing the ridge lines (c.f. Fig. 1 d)). We determine the characteristics of these lines using a probabilistic Hough transformation (e.g. Duda and Hart, 1972; Kang et al., 1991), which yields the locations, lengths, and orientations of lines contributing to the total structure. The advantage of this approach is the sampling of arbitrary lengths and orientations by

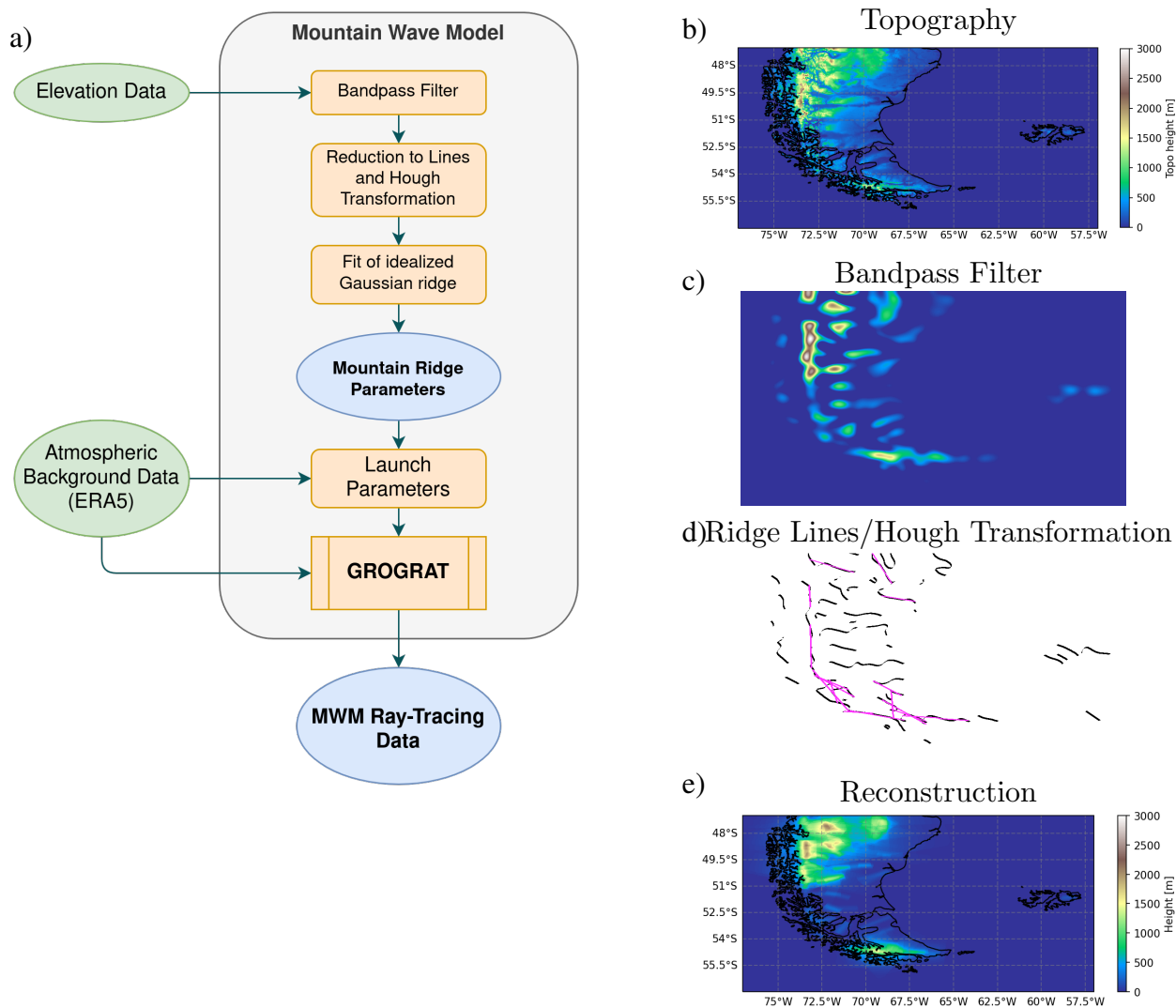


Figure 1. Flowchart of the algorithm and the intermediate steps exemplified for South America. Panel a) – Flowchart describing the main steps of the Mountain Wave Model. Input data is shown in green, internal processing steps in yellow and MWM output in blue. Panel b) - e) – example of the intermediate steps and output of the source detection algorithm [for the scale interval \[80 km, 150 km\]](#). b) – input topography data, c) – bandpass-filtered topography on an equidistant grid, d) – reduction to the ridge lines and Hough transformation for a single direction and scale. Black lines represent the detected ridge lines of the bandpass filtered field, magenta are the found straight line segments from the Hough transformation. [The considered direction here is South-West to North-East.](#) And e) – reconstruction of all fitted idealized mountain ridges.

the same method. For completeness, the Hough transform as well as its probabilistic variants and their sensitivity to parameters are briefly described in [the App.B.](#)

After the line-like features in the bandpass-filtered topography have been identified, the width and height of each possible mountain ridge at the line's location and orientation is estimated by a fit of an idealized Gaussian-shaped mountain. Note that the location is taken from the lines found by the Hough transformation while the fit itself is performed on the bandpass-filtered topography. The ~~cross-section~~ cross-section of the idealized Gaussian ridges is given by:

$$185 \quad f(x; h, a) = h \exp\left(-\frac{x^2}{2a^2}\right) \quad (1)$$

with x being the distance perpendicular to the ridge line and h and a parameters for the mountain's height and width, respectively. The fit minimizes the mean absolute error and is performed with a 2D ridge, constructed by extending this ~~cross-section~~ cross-section for the length of the line, which was determined by the Hough transformation.

As a result of the combined ~~ridge-finding~~ ridge-finding algorithm we obtain a set of ridges with the following parameters:
 190 ridge length L and ~~location X, Y , angle with respect to the equator of local Cartesian ridge coordinates X and Y (representing ridge location in zonal and meridional directions, respectively), angle between X axis and the ridge θ~~ and the best-fit, best-fit width a and, and best-fit ridge height h .

The previous step results in a collection of mountain ridges. We assume that each of these ridges can excite a MW. In order to propagate the wave with GROGRAT we need wave vector and wave amplitude. The ~~amplitude is taken as half the height displacement amplitude is calculated from the best-fitting idealized mountain height h found from the best-fitting idealized mountain, which results in the displacement amplitude $\zeta = \frac{h}{2}$ as $\zeta = \frac{h}{\sqrt{2\pi}}$. The factor $\frac{1}{\sqrt{2\pi}}$ stems from linear modeling of a two-dimensional ridge with Gaussian shape (e.g. Nappo, 2012).~~
 195 The horizontal wave vector is chosen perpendicular to the ridge orientation and the horizontal wavelength is set to $\lambda_{\text{hor}} = 2\pi a$, where a is the width of the best-fitting best-fitting idealized Gaussian ridge. This is the wavelength of maximum response for the given mountain shape (c.f. Nappo, 2012), i.e. the strongest mode of all possibly excited GWs, and gives an approximation of the full spectrum with a single monochromatic GW. Lastly,
 200 the vertical wavelength can be found from the dispersion relation and background data (see e.g. Fritts and Alexander (2003)), which is taken care of by the ray-tracer. In the specific simulations, a single MW is launched at the center of each mountain ridge at every simulated time step (i.e. every 6 hours in the global and every hour in the Southern Andes case) with launch parameters derived from the corresponding atmospheric conditions. An overview of all parameters estimated for each MW by
 205 the MWM is given in ~~Tab.~~ Table 2.

Using overlapping latitude slices, we sample the same topography more than once. In addition, it is not guaranteed that a single mountain ridge results in only one straight line in the Hough transformation. Thus, we expect redundancies in the ridge collection at this stage. In order to avoid double counting, we test each ridge against all other ridges by the following criteria:

- horizontal wavelength differs by less than 20%
- 210 – orientation differs by less than 22.5°
- distance parallel to the ridge is no more than $0.5L$
- distance perpendicular to the ridge is no more than $0.5\lambda_{\text{hor}}$

Table 2. Parameters derived within the Mountain Wave Model – either directly from topography data or from other parameters

Parameter	Description	Estimation
L	Ridge length	from Hough transformation
X, Y	Lon, lat position	from Hough transformation
θ	Math. angle of ridges w.r.t. local x-coordinate	from Hough transformation
a	Width of idealized ridge	from Gaussian fit
h	Height of idealized ridge	from Gaussian fit
λ_{hor}	Horizontal wavelength	$2\pi a$
ζ	Displacement amplitude	$\frac{h}{2} \frac{h}{\sqrt{2\pi}}$

If for any ridge pair, all of these criteria are fulfilled, they are assumed to describe the same underlying ridges and only the one with the better fit to the bandpass-filtered topography is used. After this filtering, we end up with the final mountain ridge database.

3.2 Ray Tracer

Based on the mountain ridge database established in Sect. 3.1, this section describes the derivation of MW launch parameters for specific atmospheric conditions and details of the propagation calculation within the ray tracer GROGRAT (Marks and Eckermann, 1995). Here, we use a modified version of GROGRAT that accounts for the spherical geometry along the ray paths as derived by Hasha et al. (2008). Since we are considering mountain waves, the ground-based frequency of all our waves is assumed to be zero at launch, $\omega_{gb} = 0$, which in turn leads to the intrinsic frequency $\omega = -kU - lV$, where the zonal and meridional background winds, U and V , and the horizontal components of the wave vector, k and l , are determined by atmospheric background data and the MWM respectively. Positive/negative ω corresponds to waves propagating against/with the wind. Since MWs are only excited propagating against the wind flow, we will assume positive ω in the following.

To account for surface friction of the low-level wind and potential blocking at low speeds, a reduced, effective displacement amplitude is calculated following the discussion in Barry (2008, pp. 72-82) and assuming that the displacement amplitude of a GW, who states that the conversion factor between kinetic and potential energy due to surface friction effects is about 0.64. In addition, the amplitude of the displacement excited by air forced upward is vertically over the Gaussian mountain is assumed to be about half the air parcels total vertical displacement:

$$\zeta_{\text{eff}} = \min \left(\zeta, \frac{0.32U_{\text{par}}}{N}, \frac{0.32U_{\text{par}}}{N} \right), \quad (2)$$

where N is the Brunt-Väisälä frequency and U_{par} is the horizontal wind velocity projected onto the wave vector. This means that the displacement amplitude is reduced in case the wind and stability do not allow for the full amplitude the mountain could excite. Using this effective displacement, the wind amplitude, U_{amp} , can be calculated following linear theory (e.g. Fritts

and Alexander, 2003) via

$$235 \quad U_{\text{ampamp}} = \frac{N}{\sqrt{1 - \left(\frac{f}{\omega}\right)^2}} \zeta_{\text{eff}}. \quad (3)$$

Here, f is the Coriolis parameter and ω is the intrinsic frequency of the considered GW.

The ray-tracing of the excited GWs itself is performed by [\(a modified version of\) GROGRAT](#) (Marks and Eckermann, 1995), which implements the ray equations derived in Lighthill (1978) [including corrections for spherical geometry as derived by Hasha et al. \(2008\)](#). Refraction and propagation are calculated using the equations

$$240 \quad \frac{dx_i}{dt} = \frac{\partial \omega}{\partial k_i} \quad \text{and} \quad \frac{dk_i}{dt} = -\frac{\partial \omega}{\partial x_i}, \quad (4)$$

where x_i, k_i are the i -th component of the [spherical position- and wave-vector/wave vector](#), respectively. The derivative $\frac{d}{dt}$ [is the standard Lagrangian derivative](#) $\frac{d}{dt} = \frac{\partial}{\partial t} + c_{g,i} \frac{\partial}{\partial x_i}$, where summation over i is implied, [is the Lagrangian derivative for an observer following the GW with its group velocity](#) and ω is the intrinsic frequency given by the dispersion relation

$$\omega^2 = \frac{N^2(k^2 + l^2) + f^2(m^2 + \frac{1}{4H^2})}{k^2 + l^2 + m^2 + \frac{1}{4H^2}}. \quad (5)$$

245 Here (k, l, m) are the components of the [wave-vector/wave vector](#) and H [the scale height is the atmospheric density scale height](#) ($\rho = \rho_0 \exp(-\frac{z}{H})$). GROGRAT takes into account background fields varying in space and time, allowing for 4D ray-tracing of GWs. The background fields (cf. Sect. 2.2) are internally interpolated to the current ray location using precalculated cubic spline coefficients. This allows for efficient calculation and avoids discontinuities in the background variables and their derivatives.

250 The dispersion relation in Eq. 5 is derived for small-amplitude waves in a slowly varying background flow and neglecting vertical wind. Acoustic waves are neglected [for the derivation and within the derivation of](#) the Boussinesq approximation [is used](#). [However, in the final calculations, the wave amplitude grows with decreasing density as usual](#). For the full theory, see (e.g. Nappo, 2012; Fritts and Alexander, 2003).

[GROGRAT implies conservation](#) [For the prediction of GW amplitudes along the ray path, GROGRAT considers the vertical flux](#) of wave action density, $A = \frac{E}{\omega}$, [along each ray's path except for wave saturation and for a term parameterizing radiative and turbulent damping:-](#)

$$\frac{dA}{dt} + \nabla \cdot (A \mathbf{c}_g) = -\frac{2A}{\tau},$$

[, \$F = c_{g,z} A\$, where \$A\$ is the wave action and \$c_{g,z}\$ the vertical component of the group velocity. The corresponding equation is given by \(Marks and Eckermann, 1995, Eq. 4\):](#)

$$260 \quad \frac{dF}{dt} = -\frac{2}{\tau} F - F c_{g,z} \nabla \cdot \mathbf{j}, \quad (6)$$

where $\mathbf{e}_g \cdot \mathbf{c}_g = c_{g,z} \mathbf{j}$ is the wave's group velocity and τ the parameterized damping time scale. The last term on the right-hand side is neglected since it would need evaluation using a "ray tube" technique, which is not implemented in GROGRAT (c.f. Marks and Eckermann, 1995; Lighthill, 1978). A more precise consideration using conserved wave action along the path requires a much more involved description of the wave packet in full phase space (c.f. Muraschko et al., 2015). For an estimation
 265 of the error introduced by neglecting of the last term, we approximate it locally from background fields and compare the results to standard GROGRAT in App. D. The following calculations of this study are done with the standard GROGRAT amplitude calculation. In addition, GROGRAT might in principle suffer from occurrence of caustics (e.g. Lighthill, 1978), which, however, do not strongly affect the simulated amplitudes as discussed by Hertzog et al. (2002).

Damping due to turbulence of the background is based on approaches presented in Hines (1960) and Pitteway and Hines
 270 (1963), depending on the inverse Prandtl number and the background diffusion coefficient (the vertical profile of which is taken from the approximation in Hocking (1991)). Radiative damping terms are taken from Zhu (1993).

In this study, we use the implementation of the saturation scheme described in Fritts and Rastogi (1985). This takes vertical dynamical (Kelvin-Helmholtz) instability, which is especially relevant for low-frequency-low-frequency waves, and convective instability, where the waves-wave's local temperature perturbations break vertical stability, into account.

275 For more details on the inner workings of GROGRAT, see Marks and Eckermann (1995) and Eckermann and Marks (1997).

3.3 Representation of ray-tracing data

For the analysis and discussion of Sect. 4 and Sect. 5, ray-tracing data generated by the MWM is presented using two approaches: as residual temperature structures, i.e. the temperature perturbations associated with the GWs, and as momentum flux distributions. The post-processing-post-processing steps to generate these data sets from model output are described in this
 280 section.

3.3.1 Residual temperature reconstruction

For the residual temperature fields, we aim to reconstruct GWs and their temperature perturbation on a specified spatial (x, y, z) grid for a selected time t for all considered rays, i.e. as a superposition of all predicted MWs. In particular, for the selected time t all rays that are still propagating (i.e. launched before but not yet terminated) at this time are considered. Each individual ray-
 285 trace is represented by a wave packet centered around the ray-path position of the reconstruction time. The parameters needed for this reconstruction, that is spatial location, wave-vector, phase wave vector, phase, and amplitude, are linearly interpolated to the selected time. The phase at a given point of the spatial reconstruction grid is calculated via

$$\phi_{\text{tot}} = \phi + k_{\text{hor}} d_{\text{along}} + m d_z + \frac{c_m}{2} d_z^2. \quad (7)$$

Here k_{hor} and m are the horizontal and vertical wave-numberwavenumber, d_{along} is the horizontal distance from the center of
 290 the GW in direction of the wave-vector-wave vector and d_z the vertical distance of the corresponding grid point to the rays ray's location. ϕ is the current phase at the ray-path of the wave given by the ray-tracer. This phase is calculated by GROGRAT via integrating $\phi(t, x_i)$ from launch to the current position along the ray path (Marks and Eckermann, 1995). The last term

accounts for linear frequency modulation in a linear approximation of the change in vertical wavelength along the vertical with chirp rate $c_m = \frac{\Delta m}{\Delta z}$, which is calculated as the finite difference derivative of m for the closest time steps around target altitude z . The linear approximation of the dependence of the vertical wavelength on altitude increases the reconstruction performance significantly where it changes rapidly, e.g. below critical layers (e.g. Nappo, 2012).

The spatial extent of the wave packet perpendicular to the wave-vector wave vector is estimated using the length l of the ridge exciting the MW. In this direction, the amplitude is scaled with an additional symmetric Butterworth function with 1/2 6th-order Butterworth function, $(1 + (x/S)^2)^{-1/2}$, with $S = l/2$ as scale for a smoother transition to zero at the edges. In the direction of the horizontal wave-vector wave vector, a Gaussian-like envelope with $\sigma = \frac{\lambda_{\text{hor}}}{2}$ is applied. Likewise in the vertical direction a Gaussian with $\sigma = \frac{\lambda_z}{2}$ is used. The total contribution of a single wave packet is therefore given by

$$T = -T_{\text{amp}} \cos(\phi_{\text{tot}}) \frac{1}{\sqrt{1 + \left(\frac{2d_{\text{perp}}}{l}\right)^2}} \exp\left(-\left(\frac{2d_{\text{along}}}{\lambda_{\text{hor}}}\right)^2 - \left(\frac{2d_z}{\lambda_z}\right)^2\right), \quad (8)$$

where T_{amp} is the temperature amplitude given by the ray-tracer, d_{along} , d_{perp} and d_z are the horizontal distances along and perpendicular to the wave vector and vertical to the location given by the ray-tracer. λ_{hor} and λ_z are the interpolated horizontal and vertical wavelengths, respectively. Note that the waves start with a cold phase directly above the mountain where the integrated phase along the ray is $\phi_{\text{tot}} = 0$.

There are a few uncertainties introduced by the simplifications that have been made in this reconstruction of temperature perturbations. For one, in Eq. 7, the horizontal change of wavenumbers k , l , and m is neglected, since only the vertical change can be calculated reliably from a single ray path. In addition, the vertical change of horizontal wavenumbers has been neglected, because the vertical change in vertical wavenumber dominates here (especially when approaching critical levels (e.g. Nappo, 2012)). In addition, the change of the shape of wave packets is not considered here as their footprint is assumed to be rectangular at all times. Due to the horizontal extent of some wave packets and the horizontal shear of group velocities, this is only correct in a first approximation, but since the exciting mountain ridges, in general, are of limited length this approximation is reasonable.

The total temperature perturbation, i.e. the total distribution of residual temperatures, is taken as the superposition of all these individual fields for all ray-traces.

3.3.2 Momentum flux

For comparisons with satellite and other model data, GWMF of all rays has to be expressed as a superposition on a regular spatial grid. Similar to the residual temperature, the wave parameters of the rays are interpolated to the considered time and the momentum flux of each wave packet is distributed.

The spatial distribution of the pseudo momentum flux (further also referred to as GWMF) is performed across the specified data grid using the same wave packet assumption as for temperature perturbations in Eq. 8 analogously for GWMF, but omitting the phase term and using a faster decay. The maximum pseudo momentum flux of the wave, F_{max} , is given by the raytracer (Marks and Eckermann, 1995), but can also be calculated from the temperature amplitude following the relation given by

325 Ern et al. (2004). They state $\text{GWMF} \sim T_{\text{amp}}^2$ and therefore the GWMF of a wave packet, F , has to decay faster than the temperature perturbation (by a factor of 2), since $\text{GWMF} \sim T^2 \cdot 2$. The oscillating term, $\cos \phi_{\text{tot}}$, has to be dropped because F depends only on the amplitude and not the phase. As in Sec. 3.3.1, the edges of the wave packet are smoothed with the same 6th-order Butterworth function. The resulting equation in analogy to Eq. 8 is then given by:

$$F = F_{\text{max}} \frac{1}{\sqrt{1 + \left(\frac{2d_{\text{perp}}}{l}\right)^{12}}} \exp\left(-2 \left(\frac{2d_{\text{along}}}{\lambda_{\text{hor}}}\right)^2 - 2 \left(\frac{2d_z}{\lambda_z}\right)^2\right). \quad (9)$$

330 The size of a wave packet is finite compared to the 1D trajectory given by the ray-tracer and a single ray may contribute to several grid cells of the regular target grid. On the other hand, if a grid cell is larger than the wave packet, only a fraction of the grid cell is covered and this has to be taken into account by normalization. In order to account for this effect, we are supersampling the GWMF of each wave on a finer grid (here on a 3×3 subgrid resolution for each grid point, which suffices to sample even the smallest scale waves of this study) and averaging over the finer grid points within each original grid box.

335 This gives us a numerical approximation of the grid cell integrated GWMF. Since we are interested in the GWMF density, we divide the total contribution by the grid ~~cells~~-cell's area:

$$F_{\text{tot}} = \frac{F_{\text{grid}}}{A_{\text{grid}}} = \frac{\int F dA}{A_{\text{grid}}}, \quad (10)$$

where F_{tot} is the wave's contribution to the GWMF density distribution, F_{grid} is the GWMF in the corresponding grid cell, the integration is across the (horizontal) area of the grid cell and A_{grid} is the ~~footprint of the grid cells of the horizontal distribution~~total horizontal surface area of the corresponding grid cell in the data grid.

340

The total GWMF density distribution is again calculated by summing up the single contributions of every ray-traced wave packet for each time step.

4 Model Validation

In this section, we validate the MWM presented in Sect. 3 in two different ways. First, we investigate the performance of describing the underlying topography and its structures by the idealized ridges and second, we look at the resulting temperature residuals of MWM predicted mountain waves in comparison to ECMWF IFS data.

345

4.1 Detected structures and scales in the MWM

To investigate the capability of the MWM to adequately represent the topographic structures, we show a comparison of the underlying elevation to small (≤ 150 km) and large scales (>150 km) of detected ridges in Fig. 2. Although a perfect ~~reconstruction~~reconstruction of the underlying topography is not what we wanted to achieve with the MWM, the ~~ridge-like~~ridge-like mountain chains should be represented by the model. Our algorithm of fitting idealized ridges of various scales and sampling in four directions implies that a single topographic feature could be captured multiple times. This is especially the case for very

350

~~large-scale~~large-scale and plateau-like features. Therefore, the elevation height of the reconstruction might be higher than the topography itself.

355 Higher values in absolute (superposed) terrain height ~~does~~do not inevitably lead to an overestimation in GW activity. For example, if there are two ridges lying on top of each other at a right angle, depending on the wind, only one of both ridges will excite a GW. Therefore, the correlation ~~of~~between terrain height and GW temperature amplitude is not as straightforward.

Figure 2a shows the true elevation of the terrain of South America, while panels b and c show the small and large scales detected by the MWM, respectively. The reconstructions are generated by superposing all found ridges linearly. The ~~small~~small-scale ridges are located mainly in the main north-south oriented mountain ridge where we would expect them, but additionally, there are also quite a few in the east and at the tip of Tierra del Fuego with an east-west orientation. These eastern ridges can also be found in the topography itself. The general structure represented by the small scales agrees well with what we see from the topography. The large scales form a broad ridge-back along the Andes with a maximum above the highest elevation of the southern Andes around 50°S and another one to the north, where the topography shows a ~~large-scale~~large-scale plateau-like elevation, that is sampled along multiple directions and therefore more pronounced in the reconstruction.

In Fig. 2d, the elevation profile of the east coast of the USA including the Rocky Mountains is shown. Again, panels e and f show the detected small and large scales, respectively, as detected by the MWM. This case poses a more difficult problem for the MWM due to the topography being even more complex. While South America exhibited ~~ridge-like~~ridge-like features reaching down to sea level from the start, the Rocky Mountains are already located on top of a very ~~large-scale~~large-scale elevation feature. Nevertheless, the ~~small-scale~~small-scale ridges represent elongated mountain chains, like for example the Sierra Nevada and Baja California, well and the structures can be matched to the topography. A more scattered structure is seen in the ~~large-scale~~large-scale features. Increased elevation is found above high mountain ranges, like the Rocky Mountains, Sierra Nevada, and Sierra Madre Occidental. Again the topography is well represented by the identified idealized mountains.

The different scales of the detected mountain ridges and their ~~spread~~distributions are shown in Fig. 3 for South America and the Rocky Mountains. Both cases are very comparable in their general distribution of ridge height, length, and horizontal wavelength. The MWM detects mostly ridges with small lengths between ~~~7540~~~7540 km and ~~150200~~150200 km. Although there are a few outliers with lengths of up to ~~~500400~~~500400 km, a natural topography is not easily described by straight ridges due to curving or bends in the mountain structure. Thus the longer ridges are usually only detected for the largest scale, low amplitude features (high amplitudes are only expected for plateau-like topography). Ridge heights are almost evenly distributed in a range of ~~~100 m to 600 m~~~100 m to 600 m and ~~extending~~extend up to 800 m. The distribution is minimally shifted towards higher ridges in the Rocky Mountain case (Fig. 3b) accounting for the higher elevation in this region. Considering the horizontal wavelengths of the detected ridges, they are evenly distributed between ~~10070~~10070 km and ~~~400300~~~400300 km with sparser distribution ~~up to 1150~~up to 1150 for longer scales up to 1250 km. This can be attributed to the small scales in general being of shorter length as well and thus, they do cover not as much area and multiple ridges are needed for the description of the topography. The ~~larger-scale~~larger-scale ridges on the other hand cover a large area and ~~less~~fewer of them are needed for a similar region.

In conclusion, the ~~investigation of detected elevation features by the MWM does a good job in representing features of various scales~~MWM detects and represents orographic features of the elevation of various scales under consideration that

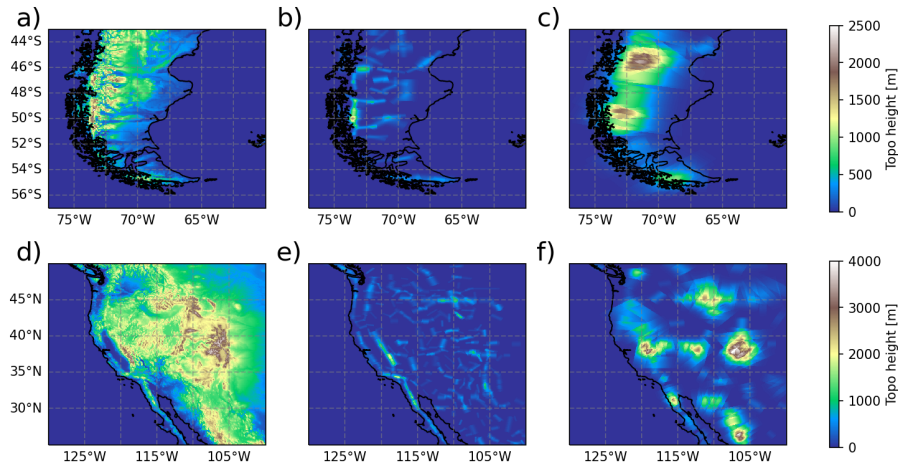


Figure 2. Comparison of the underlying topographic data (a and d) to the reconstruction from all idealized Gaussian mountain ridges identified by the MWM (b, c, e and f). Panel a, b and c show the Southern Andes region, panel d, e and f the west of North America. The reconstruction is separated into small scales (≤ 150 km, panels b and e) and large scales (>150 km, panels c and f).

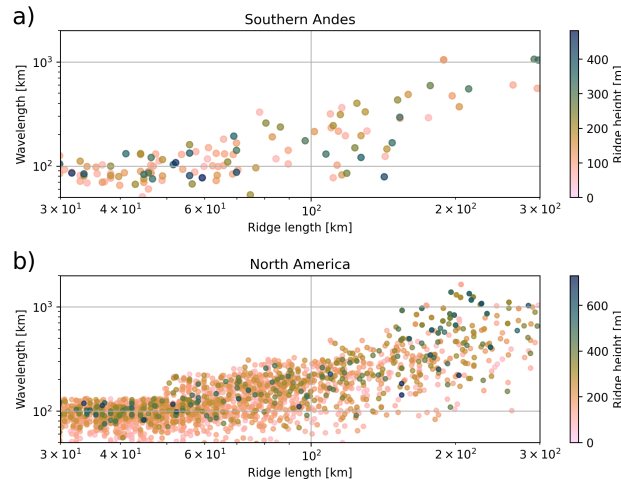


Figure 3. Scales of detected ridges that contribute to the approximation of the Southern Andes region (Fig. 2b and c) and western North America (Fig. 2d and e). The histograms for ridge scatter shows the length in km (pink), of the ridge height in m (green) and versus the main horizontal detected wavelength in km (blue, cf. Sect. 3.1) are shown and the corresponding height in color shading. Note the logarithmic scales on both axes.

the representation of elevation data by two-dimensional ridges has some intrinsic problems (especially with isotropic and plateau-like features). Although this is no indication of whether we cover all relevant scales, it provides confidence in the

390 underlying ridge detection algorithms as a tool to extract the main MW sources and the corresponding parameters.

4.2 Residual temperature as compared to ECMWF operational analysis data

Figure 4 compares the residual temperature due to gravity waves taken from ECMWF IFS operational analysis data on 21.09.19 at 06:00 UTC to a reconstruction estimated from MWM data. ~~The As described in Sect. 2.2, the IFS data set has been detrended-scale separated~~ in the same manner as the ERA5 data used for ray-tracing backgrounds(see Sect. 2.2); ~~only, only that~~ now we are interested in the remaining residual fields representing ~~small-scale-small-scale~~ gravity wave perturbations instead of the background. ~~The operational analysis data set is provided on a 0.1° resolution and capable of resolving mesoscale gravity waves~~In the considered region, the resolution of 0.1° corresponds to a horizontal resolution of about 10 km meridionally and 6 km zonally. We estimate the smallest scale GWs resolved in the data set to be about 80 km horizontal wavelength by the scale, where the energy spectrum deviates strongly from a slope of k^{-3} (c.f. Skamarock, 2004). The reconstruction of residual temperature from the MWM is described in Sect. 3.3.1.

First, we consider the residual temperatures below the tropopause at an altitude of 8 km (Fig. 4 a and b). At this altitude, we do not yet expect strong horizontal propagation of ~~smaller-scale-smaller-scale~~ MWs, which typically starts to become relevant above the tropopause, thus we expect the MWM to exhibit GW patterns close to the main mountain structures. The IFS data shows high activity of all scales above the oceans as well at this height, which indicates either wave sources other than orography (e.g. convection, ~~spontaneous adjustment, jet fronts~~jet fronts, and geostrophic (or spontaneous) adjustment, where an out-of-balance jet radiates excessive energy as inertia-gravity waves (e.g. Fritts and Alexander, 2003; Williams et al., 2003; de la Camara et al., 2019) or completely different tropospheric processes, that our scale separation anomalously picks up. However, the MWM also shows a large-scale pattern to the east of the continent, which might indicate that orographic GWs of large-scale (and therefore higher horizontal group velocity) might also add to the patterns seen in the IFS. Above the Andes, we see the typical north-south oriented wave fronts and an enhanced region of ~~small-scale-small-scale~~ perturbations at around 50°S , 74°W in both data sets. The warm temperature phase follows the coastlines in both data sets. The MWM also shows trailing waves at the tip of Tierra del Fuego, which are oftentimes seen in temperature observations of this region (e.g. Preusse et al., 2002; Jiang et al., 2012; Kruse et al., 2022). ~~There is also a large-scale pattern eastward of the continent, which can be associated with a similar pattern in the IFS data. However, we cannot be sure whether the pattern in the model arises from orography.~~ Both data sets agree in terms of the magnitude of temperature amplitudes.

At 20 km altitude (Fig. 4d and e), we expect to observe at least some oblique propagation of MWs due to stronger winds and wind gradients. Still, both data sets show the ~~east line following warm phase followed by warm phase following the coastline, with~~ trailing waves in the south. The highest amplitude residuals are found in the same location of $\sim 42.5^\circ\text{S}$, which is in the lee of the highest elevation topography. In terms of structure, both show a ~~large-scale-large-scale~~ pattern interfering with ~~smaller-scale-GWs~~. The IFS, however, seemingly does a better job of resolving very small scales-GWs of significantly shorter wavelengths than the main structure, about 100–150 km and smaller. Features of very short scales (i.e. below about 60 km) are not as well represented by the MWM temperature reconstruction as by the IFS, which is partly due to the lower scale limit set to 80 km. Above the Falkland Islands, both show GWs that propagated towards ~~towards~~ the east, the GWs of the MWM are of relatively low amplitude, while the IFS shows higher amplitude and ~~larger-scale-larger-scale~~ waves.

425 At 30 km altitude, the polar vortex turns from mainly eastward to a more north-eastward direction above the Andes. This leads to a change in the horizontal wind gradients, and in turn to GWs refracting and turning as well (Fig. 4g and h). Both data sets show gravity waves mainly facing to the south-west instead of westward, as a consequence of horizontal refraction towards the stronger winds in the ~~south-east~~ (Krasauskas et al., 2022). ~~We see significant GW activity over both the Pacific Ocean as well as southeast~~ (Krasauskas et al., 2022). ~~The MWM predicts significant MW activity above the Atlantic Ocean in the IFS data, which can be mostly explained by oblique propagation of MWs from the Southern Andes as indicated by the MWM data. The amplitudes of the waves, which is (mostly) stemming from the main Andes mountain ridge and has propagated to the east. These patterns are confirmed by the IFS data, which shows a large connected band of GWs above this region. The MWM does not show such high continuity due to the (short) mountain ridge approximation and reconstruction from single wave packets. Nevertheless, the phases of different wave packets fit well together and a coherent structure is seen. Propagation to the west is~~
430 ~~only faintly~~ predicted by the MWM ~~agree with the IFS. The IFS model also shows large-scale waves above the Pacific Ocean, which are not present in the MWM, while the IFS data shows strong GWs far above the ocean.~~

We analyzed the spectral characteristics of the waves around 45°-50°S, 60°-66°W in Fig. 4g ~~at 30 km altitude~~ using the S3D technique (3D wave fitting in a subdomain, previously used by e.g. Preusse et al. (2014); Geldenhuys et al. (2021); Krasauskas et al. (2022)). S3D returns estimates of the 3D wavenumber (k, l, m) which are then used as input for a reverse ~~ray tracing~~ ~~ray-tracing~~ calculation using GROGRAT. This calculation suggests that these waves originate in a region with ~~large scale~~ ~~large-scale~~, low elevation topography leeward of the main Andes ridge ($\sim 49^\circ - 51^\circ\text{S}$, 70°W in Fig. 4). Since this topography is "~~plateau-like~~ ~~plateau-like~~" it is missed by our ridge finding algorithm (not shown). It is also possible that these waves were excited by orographically-linked convection, which was observed by Worthington (e.g. 2002, 2015). These processes are currently not accounted for in the MWM. ~~Smaller-scale~~ ~~Smaller-scale~~ features in the northern part are represented correctly in
445 the MWM both in terms of orientation and amplitude. Also, both models show ~~small-scale~~ ~~small-scale~~ fluctuations at around $\sim 50^\circ\text{S}$, 73°W .

Figure 54c, f and i shows the wind situation at this time. We see a turning wind with altitude: while the wind is passing the Andes mostly eastward below 20 km, the wind turns ~~to~~ north-north-east above. Thereby GWs are refracted and the phase fronts change alignment to north-west to ~~south-east~~ ~~southeast~~. The turning of GWs in the ~~Southern Andes region (same as in~~
450 ~~Fig. 4) within the~~ MWM can be seen in Fig. 5, ~~which accounts for all GWs launched between 20.09.19 00:00 and 21.09.19 23:00 with each mountain ridge launching a single GW every hour.~~ Although there are MWs launched with various directions between southward and westward, at around 25 km altitude, ~~most of the MWs turn south-westward, leading to this being the dominant wave orientation. This also implies that the change in wave field characteristic is not happening due to filtering, i.e. breaking (e.g. at a critical level) and thereby reduced visibility,~~ of westward facing GWs, but instead due to refracting GWs in
455 the turning wind profile.

In comparison to the ~~high-resolution~~ ~~high-resolution~~ IFS simulations, the MWM does perform quite well, if we consider the simplicity of the approach. Of course, we do not expect the MWM to represent the exact structure of the IFS, since nature is more complex than this superposition of linear 2D-like MWs can account for. The aim of the MWM is to predict the horizontal propagation in a comprehensive way allowing for ~~an~~ ~~a~~ straightforward investigation of propagation paths and momentum

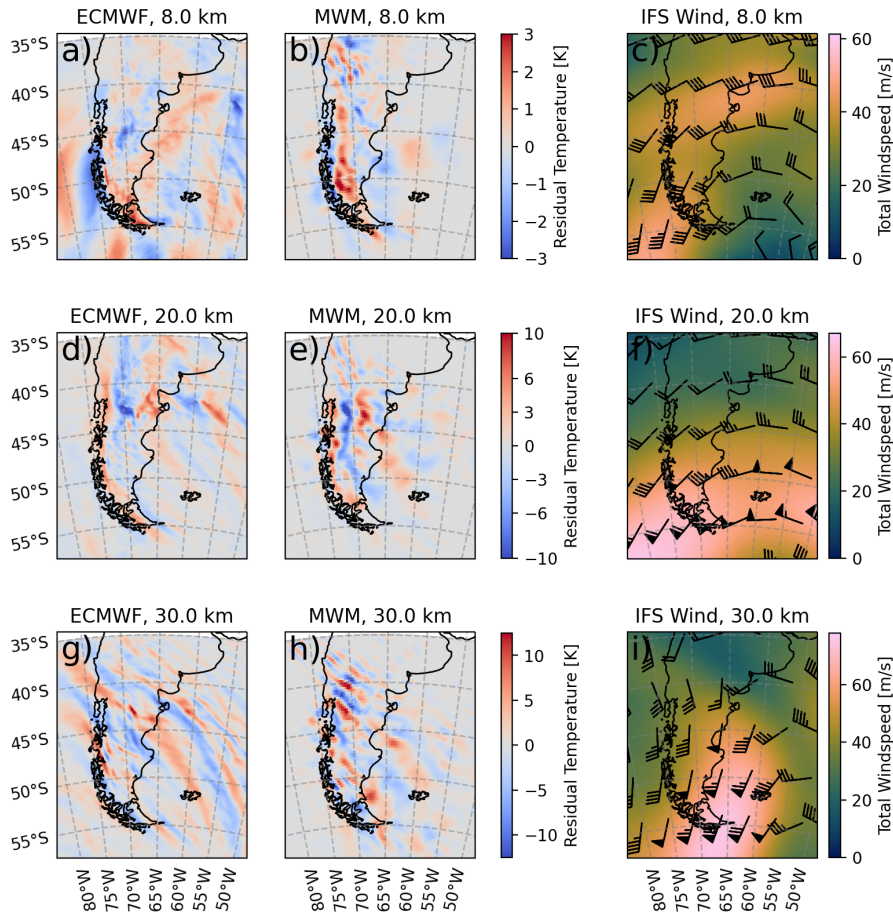


Figure 4. Temperature residuals from ECMWF IFS operational analysis data for 21.09.21.19 06:00 UTC (left column) and the corresponding reconstruction from MWM data at the same time (middle column). Horizontal cuts are shown at altitudes of 8 km, 20 km and 30 km in the top, middle and bottom row respectively. Note the differing color scales between different altitude levels. Synoptic wind fields as predicted by the IFS are shown on the right column, where colorshading gives the total wind speed and wind barbs show the wind direction.

460 transport [patternpatterns](#). We have seen that the model is capable of doing so and therefore is a useful tool to estimate MW residual temperature structures. Especially the GW field characteristics, like turning and propagation of momentum, are captured quite well, and therefore the MWM can be used to investigate GW parameters of observations and propagation patterns in the following section.

5 Prediction of global GWMF distributions

465 In the following, we use the MWM and it's GWMF predictions to explain some observational features of monthly mean HIRDLS satellite data via investigation of the GW parameters and wind profiles, i.e. GW filtering due to wind conditions [that](#)

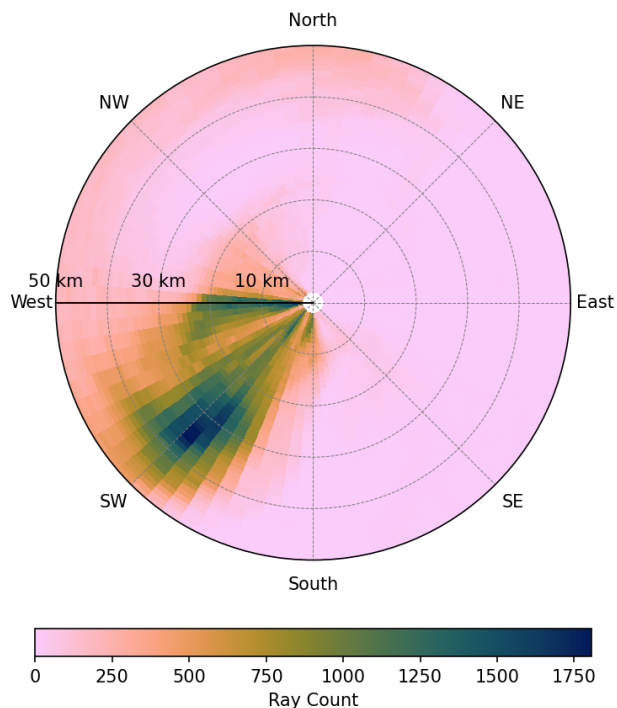


Figure 5. Directional-Direction vs. altitude distribution of MWs as modeled by the MWM in the Southern Andes region (same as in Fig. 4). This considers all GWs launched between 20.09.19 00:00 and 21.09.19 23:00 with each individual mountain ridge launching a single GW every hour. The radius gives the altitude of a given MW, angle gives orientation of the wave vector. The color-shading gives the total count of rays for a given altitude-orientation bin. There is a clear trend for GWs to turn to south-west at around 25-30 km. Although the sum over all orientations for a given altitude is monotonically decreasing with altitude, there is a maximum at around 35 km with south-west oriented GWs.

lead to a critical level for MWs. In particular, we try to answer the question of why there is not as much GW activity seen by satellites as expected above the Himalaya and the Rocky Mountains. AfterwardsAfterward, we look into predicted orographic GWMF throughout the year, which agree-agrees with previous studies of MW propagation. Here, the MWM predicts strong
 470 year-round horizontal MW propagation.

5.1 Global distributions of momentum flux

HIRDLS in general does not show strong GW activity above the Himalaya and Rocky Mountain region in January (Ern et al., 2018), contrary to the general observationunderstanding, that mountain waves are able to propagate far into the stratosphere in the winter months. We will investigate possible reasons behind this in the following by comparing global horizontal distributions
 475 of GWMF retrieved from HIRDLS to predictions of the MWM at altitudes of 16 km, 20 km, and 25 km. We will also compare both data sets in terms of propagation patterns found in winter above the Drake Passage and the Southern Ocean.

The distributions retrieved from HIRDLS show gaps in the lower altitudes due to the tropopause and clouds. The former ~~removes limits observations in~~ the tropics and parts of the subtropics at 16 km and 20 km, while the latter ~~especially removes limits observations in~~ regions of subtropical convection from the data at 16 km. The satellite observations pick up
480 GW signatures of all sources. In winter these are mainly orography ~~and spontaneous imbalances~~ as well as frontal systems and jet imbalances (Wu and Eckermann, 2008; Alexander et al., 2016), in summer the main source is convection. In contrast, the MWM only shows orographic GWs, which has to be kept in mind when comparing both. In particular, this leads to possibly higher observed GWMF throughout the observations, which might not be mirrored by the MWM data. This could either suggest a different GW source, if there is no similar structure in the MWM data, or ~~an a~~ superposition of orographic and other
485 sources ~~;~~ if a feature is structurally seen in the MWM.

For a direct comparison of global GWMF distributions, we apply an observational filter that accounts for HIRDLS observation geometry (Trinh et al., 2015) to every ray of the MWM before calculating the GWMF distribution following Sect. 3.3.2 on a 1.5° resolution and bin the resulting GWMF ~~values~~ in the same way as the HIRDLS profiles in order to derive comparable global distributions (see Sect. 2.3). Two case studies for January and July 2006 are presented in this section.

490 5.1.1 January 2006

Figure 6 shows monthly mean total GWMF distributions for January 2006 as retrieved from HIRDLS (left column) and predicted by the MWM (right column) at altitudes of 16 km, 20 km and 25 km. The strongest pattern in the observations is found above the Himalaya and Altai Mountains (Mongolia), where we see two local maxima. The ~~one maximum~~ above the Himalaya dominates at 16 km, but ~~decreases in strength,~~ with increasing altitude, weakens stronger than the one above the
495 Altai mountains ~~with increase altitudes~~. Therefore, at 25 km only the pattern above Mongolia remains. This pattern is also rather consistent throughout the considered altitudes. The same structural pattern is seen in the MWM, although with lower amplitudes. Features in both regions show comparable local maxima at lower levels and, at higher altitudes, the one above the Himalaya is reduced analogously to the observations.

To understand this northward shift, we can investigate the properties of GWs in the different regions within the MWM. Fig. 7
500 shows histograms of horizontal and vertical wavelengths at 16 km, and 25 km for both regions as calculated from the MWM. We see that the horizontal wavelengths are almost the same at both altitudes and regions. Conversely, the vertical wavelengths differ strongly. The MWs of the southern region (above the Himalaya) ~~exhibits exhibit~~ longer vertical wavelengths, which are also strongly suppressed by the observational filter (with a cutoff at $\lambda_z = 12$ km) at 16 km altitude. Propagating upwards, they refract strongly towards short vertical wavelength due to a negative vertical gradient of zonal wind (see Fig. 9). There are at
505 least two possible reasons for ~~the GWs these GW features~~ missing in the satellite observations at higher altitudes ~~;~~ that are considered here: For one, the vertical resolution of HIRDLS is about 1 km (Wright et al., 2009), which, in principle, allows for the detection of GWs with a vertical wavelength as low as 2-4 km. Some waves are refracting even below this vertical wavelength and can therefore not be picked up by the instrument. Another reason ~~are~~ might be strong amplitude GWs, which are often found in this region, that could completely break instead of propagating further with an amplitude reduced below
510 the saturation limit in a strong wind vertical shear (Kaifler et al., 2015). Such a complete breakdown of GWs is currently not

captured by GROGRAT simulations. The MWM could be a suitable tool to test this hypothesis in other, more specific case studies, by implementing different breaking schemes.

515 A very strong GW signature in the MWM is seen above the Rocky Mountains. The amplitudes are overestimated in comparison to the satellite observations, ~~but~~ nevertheless a similar structure is visible. In higher altitudes, this signature is strongly reduced until it almost vanishes at 25 km. There is also a minor southward shift of GWMF towards California visible which is also ~~pieked-up~~ hinted at by the satellite data. This feature sits, however, right at the edge of the observation and is therefore not completely seen. The strong reduction in amplitude can be explained by similar arguments as for the Himalaya region: there is a strong negative vertical wind shear above the Rocky Mountains reducing the allowed amplitudes of GWs strongly. Compared to the Himalaya region, in the MWM the MWs ~~start-out~~ launch with much stronger amplitudes (about a factor of two, not shown), making them more likely to encounter saturation or complete breakdown (there is plenty of evidence of strong MWs and their breaking in this region, e.g. Guarino et al. (2018)). The latter process might be a reason for the overestimation at 16 km (the negative wind shear starts already at roughly 10 km, where waves could already break). Therefore, ~~the strong signature in the MWM data could be another hint at this or another process missing in our current understanding of GW physics~~ seen in the predictions could be an indication of a process that is not yet modeled within the MWM.

525 Another strong feature predicted by the MWM ~~are~~ is local maxima in the Southern Hemisphere above New Zealand and the southern Andes, which are matched partially by the observations. These maxima strongly decrease in higher altitudes and vanish completely at 25 km as expected, since MWs are filtered by the wind reversal at around 20 km in the summer hemisphere. The MWM prediction is stronger than the observations, which could, again, be related to the above-mentioned processes. The prediction shows strong eastward propagation above New Zealand, while the satellite data seems to show signs of strong oblique propagation eastward towards the east of both sources. However, their persistence The presence of this pattern at 25 km altitude in the observations is, however, not consistent with them being MWs as well. Instead, these are most likely of other origins.

530 In the ~~northern~~ North Atlantic region, the MWM predicts GW sources in Newfoundland, southern Greenland, Iceland, and Scandinavia. ~~Eastward propagation~~ Strong eastward propagation of MWs is seen especially above Iceland, where the ~~GWMF reaches to the patch~~ pattern of GWMF merges with the feature above Scandinavia. ~~The observation shows a more complex picture with the same sources: the single features seem to merge into each other creating a continuous band of GWMF above the Atlantic, which persists into higher altitudes. At~~ In addition, the MWM predicts eastward propagation from Newfoundland towards southern Greenland at 25 km, even though the GWMF values predicted by MWM are, generally, suppressed at this altitude. The HIRDLS observations show similar, although more complex features in this region. The aforementioned MW sources are clearly visible but merge into a band of strong GW activity at 20 km ~~there is increased GWMF east of Newfoundland (compared to lower levels) hinting at GWs from sources like the jet or storms above the Atlantic ocean. Most features vanish at this altitude and only the ones close to orography and eastward of Iceland remain. In comparison to the MWM, observed features at 16 and above. This band follows the path of the polar vortex and might therefore be related to local GW sources such as jet imbalances and fronts (Geldenhuys et al., 2021). The occurrence of other sources than orography in the observations is~~

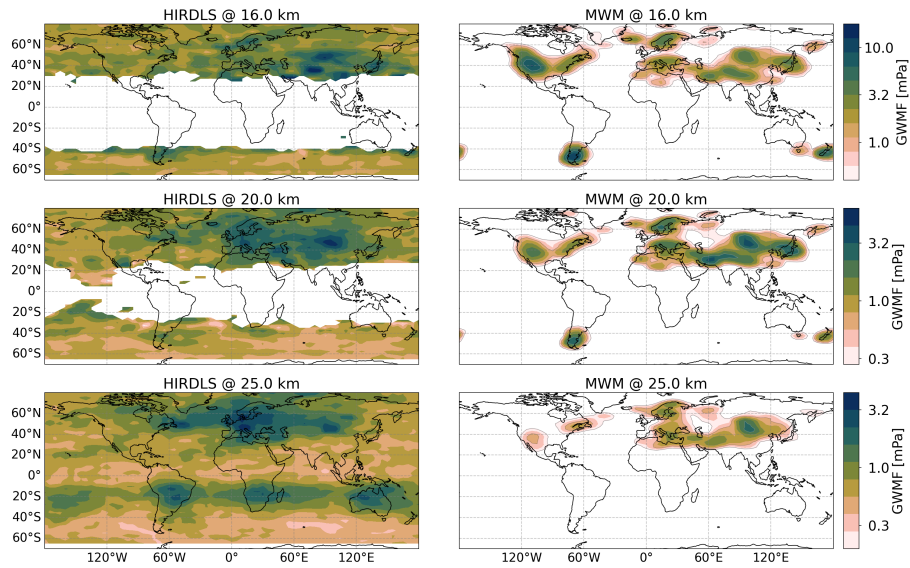


Figure 6. Monthly mean of global GWMF distribution for January 2006. Left column shows HIRDLS satellite data (see Sect. 2.3), right column shows distributions produced by the MWM. The different rows present data for 16 km, 20 km and 25 km altitude from top to bottom respectively. [Note the logarithmic color scales.](#)

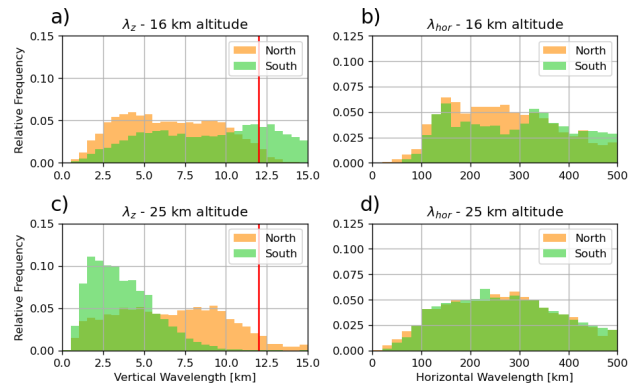


Figure 7. Distribution of vertical (left) and horizontal (right) wavelengths as found by the MWM at altitudes of 16 km (top) and 25 km (bottom). The northern region corresponds to the Altai Mountains at 42.5°-55.0°N 75°-105°E, the southern region to the Himalaya at 30.0°-42.5°N 65°-95°E. The vertical red line on the left panels marks the cutoff wavelength of $\lambda_z = 12$ km for the present HIRDLS data.

545 [strengthened by the \(slight\) GWMF increase between 20 km can therefore be attributed to orographic origin, while the ones observed at km and 25 km should have other sources \(see e.g. Geldenhuys et al., 2021\).](#)

To further investigate the reasons for the differences between the MWM and the satellite observations, we use blocking diagrams similar to the ones introduced in Taylor et al. (1993) as well as vertical profiles of horizontal wind. The regions of

interest are shown in Fig. 8. We investigate differences in propagation conditions above the Himalaya compared to Mongolia, above the Rocky Mountains, and above southern Africa, where a strong GWMF pattern arises in the HIRDLS data at 25 km altitude (see Fig. 6). For illustration of the general wind conditions, Fig. 8 shows the monthly mean zonal wind at 20 km.

In the blocking diagrams shown in Fig. 9a – d, the criterion of waves blocking-encountering a critical level whenever the intrinsic frequency of a GW goes to zero, $\omega_{\text{intr}} \rightarrow 0$, is used, with:

$$\omega_{\text{intr}} = \omega_{\text{gb}} - \mathbf{k}_{\text{hor}} \cdot \mathbf{U} \quad (11)$$

$$\Leftrightarrow \omega_{\text{intr}} = \omega_{\text{gb}} \left(1 - \frac{U_{\text{par}}}{v_{\text{ph}}} \right). \quad (12)$$

Here, \mathbf{k}_{hor} and \mathbf{U} are the horizontal wave- and wind-vector wind vector, U_{par} is the wind speed projected onto the horizontal wave-vector wave vector, and v_{ph} the horizontal phase speed of the GW. Note that the derivation of this equation requires $\omega_{\text{gb}} \neq 0$, which is not true for the considered MWs close to the launch site or in a static background.

The curve of $\omega_{\text{intr}} = 0$ is a circle in phase speed diagrams with center at $(\frac{U}{2}, \frac{V}{2})$ and radius $R = \frac{1}{2}\sqrt{U^2 + V^2}$ for zonal and meridional background winds U and V . These contours have been superposed and covers the restricted, i.e. blocked or filtered, part of the phase speed spectrum. These curves can be superposed on a phase speed diagram for all altitudes from the surface up to 25 km altitude and divided by the number of contours to give a measure of how strong or wide-spread across heights the blocking is. widespread across altitudes the critical levels are for GWs launched at the ground. This is done in Fig. 9a – d show therefore, where the color shading gives the percentage of altitude at which blocking occurs for a given (ground-based) levels, that exhibit critical levels for GWs of the corresponding (ground-based) phase speed in color shading. In other words, the color shading gives an estimate of the probability for GWs with given phase speed to be filtered by a critical level below 25 km. Note, however, that these diagrams are only an indication of blocking-for-MWs-with-critical levels for MWs near their launch location and in an approximately constant wind profile, where $\omega_{\text{gb}} \approx 0$, which are blocked. In these conditions, critical levels are encountered wherever the horizontal wind projected onto the horizontal wave-vector wave vector becomes zero. As an additional metric, the monthly mean vertical profiles of horizontal wind for the four regions are shown in Fig. 9e and f.

Comparing the blocking patterns for the Himalaya and Mongolian plateau in monthly mean winds in Fig. 9a and c, we see that a wider range of phase speeds is restricted by blocking in the southern region, above the Himalaya. This potentially leads to a stronger suppression of GWs of other origin-origins than orography, which might be part of why the GWMF in HIRDLS declines so strongly in Fig. 6. If we look at the vertical profiles of monthly mean winds, which are shown in Fig. 9e, neither of the regions show a wind reversal and thus MWs should in general propagate similarly well in both regions. However, the zonal wind of the southern region exhibits a strong vertical gradient. The wind speed peaks at around 12-13 km with a pronounced maximum of about 45 ms^{-1} , that-which is roughly 5 km below the level of maximum wind speed of the northern, Mongolian, region. This high wind speed allows for MWs of higher amplitudes, which afterwards afterward encounter a strong negative wind shear leading to refraction towards small vertical wavelengths and wave breaking due to reaching the saturation limit. Kaifler et al. (2015) suggests that high amplitude GWs reaching saturation might break completely instead of propagating further with a reduced amplitude. This total breakdown of saturating waves is not represented in GROGRAT simulations,

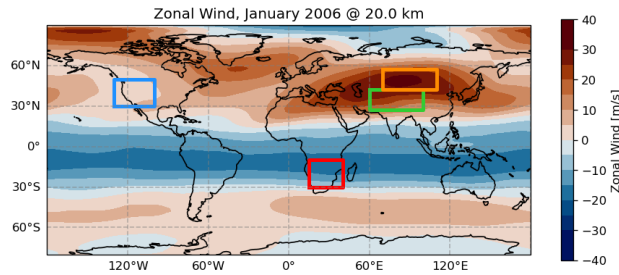


Figure 8. Regions of interest for blocking considered in this study shown on top of the monthly mean zonal wind at 20 km altitude: Himalaya (green), Mongolian Plateau (orange), Rocky Mountains (blue) and southern Africa (red). The same colors as in Fig. 7 have been used for the Mongolia and Himalaya regions.

~~but could be a reason why HIRDLS sees less~~ The lack of this effect in the GROGRAT simulations could be one reason for the enhanced GW activity above the Himalaya predicted by the MWM (Fig. 6). Above the Altai mountains, the propagation conditions are more favorable due to a more consistently strong wind, that is slowing down only above 25 km. Therefore the observations and the model do not see as strong a reduction in activity as above the Himalaya region.

Next, we want to investigate the Rocky Mountains. The blocking diagram for this region is shown in Fig. 9b and corresponding wind profiles are given in Fig. 9 f (blue lines). The blocking diagram exhibits high values at and around the origin indicating low wind speeds at various heights. The dumbbell-like shape with structures on either side of the origin ~~are is~~ a consequence of a wind reversal. This is confirmed in the wind profiles, where we see the reversal of horizontal winds at about 22 km. This reversal prevents any MW activity to propagate further upward. A possible reason for the wind reversal despite being in the winter hemisphere is the location of the polar jet. In Fig. 8 we see that the polar jet in the monthly mean is not located above the Rocky Mountains but much further north (about 75°N), which strongly affects the propagation criteria for MWs. In terms of shape of the wind profile, the situation is similar to the Himalaya region with a peak wind speed of about 25 ms^{-1} at ~ 11 km altitude followed by a strong negative wind shear. In addition, the ~~low-level~~ low-level wind speeds are around 6 ms^{-1} , which is four times as strong as in the Himalaya region. The MWs of this region ~~therefore,~~ therefore, have the potential to launch with much higher amplitudes, making them more likely to reach saturation and complete breaking due to high amplitudes as described by Kaifler et al. (2015). Since this is not represented in GROGRAT, the MWM may predict much stronger GWMF in this region, than there actually is in reality.

Lastly, we want to briefly consider southern Africa to exclude MWs as a source for the pattern seen in HIRDLS at 25 km. The corresponding blocking and wind profiles are shown in Fig. 9d and f (~~yellow-red~~ red lines). The blocking diagram has a pronounced dumbbell shape from a wind reversal, which is confirmed by the wind profiles at low altitudes (about 4 km). This makes propagation of MWs impossible. Conversely, only small parts of the phase speed spectrum ~~is-are~~ blocked. These are ideal conditions for GWs of sources that generate a wide range of phase speeds like convection (e.g. Salby and Garcia, 1987; Alexander and Dunkerton, 1999; Preusse et al., 2001; Choi and Chun, 2011; Trinh et al., 2016). Therefore we can conclude that the observed ~~pattern-patterns~~ appears not due to orography but other sources (most likely convection).

To summarize, the predictions of the MWM and the calculated wave parameters can explain the shift of focus of GW activity from the Himalaya to the Altai Mountains and therefore solve the question, of why there is not as much GW activity as would be expected from the topography itself. The MWM shows, that parts of the GW spectrum refract to very short vertical wavelengths, which makes them hard to be ~~detect~~ detected by the satellite. The refraction to smaller vertical wavelengths is distinguished
610 from GW breaking by the GW amplitudes as calculated within GROGRAT, which, in general, do not reach saturation although the vertical wavelengths shorten significantly. The feature above the Himalaya is more pronounced without the ~~instrument~~ specific ~~instrument-specific~~ observational filter. On the other hand, the MWM is showing a strong signature above the Rocky Mountains, as would be expected from the topography. Since this is not present to such a degree in the satellite data, it might be a hint at a GW process, that is not captured as of now (e.g. total breakdown of GWs reaching ~~saturation~~ saturation
615 level (Kaifler et al., 2015)). In total, the MWM has proven to be a useful tool to investigate the orographic part of GWMF observations.

5.1.2 July 2006

In the following, we are considering predictions of GWMF for July 2006 and ~~use~~ using calculated MW parameters (mainly the wave vector) to explain features found in HIRDLS ~~observations~~ observations. Fig. 10 shows global horizontal distributions
620 of GWMF as retrieved from HIRDLS (left column) and predicted from the MWM after the application of the observational filter (right column) at altitudes of 16, 20 and 25 km. The main feature in both data sets is the maximum above the southern Andes. At 16 km HIRDLS shows a strong maximum at around $\sim 52^\circ\text{S}$ accompanied by a weaker separate maximum directly north at around $\sim 42^\circ\text{S}$. In higher altitudes, the southern maximum vanishes, while the northern persists. In total, this leads to a northward shift of the global maximum.

The HIRDLS data set ~~also shows eastward propagation of GWMF from~~ shows a strong eastward spread around these maxima up to about 30°W over the Atlantic. ~~This is a hint at orographic GWs from the southern Andes contributing in this region. Although in a textbook case, we would expect the extent of the lateral propagation to increase by height, the data set shows a reduced trail at 20 km altitude and an increase above. The MWM in comparison~~ A comparison with the MWM, which
625 shows a very similar pattern with a larger maximum above the southern Andes. ~~Although the MWM does not show a clear maximum in the southern part, the pattern is rather spread out and shifted northward at higher altitudes as in the observations. In terms of horizontal GW propagation, the data shows stronger extent of the propagation the higher one looks at. At~~ shows that the observed spread of GWMF can be explained by eastward propagating MWs. In a textbook case of oblique propagation from a single source region, the extent should increase with altitude. This is true in the MWM predictions, where MWs reach as far as 30°W at 25 km, the GWMF is transported up to 30°W . The satellite observations, however, show a decrease at
630 20 km followed by an increase in spread at 25 km altitude. Although the maximum of the MWM prediction is not as precisely localized as in the ~~satellite observation~~ observations, it shows the same northward shift with higher altitude.

Using the ~~The~~ MWM allows for an ~~in-depth look of~~ in-depth look at what is causing the northward shift seen in observations by investigating individual GW parameters in these regions. Fig. 11 shows histograms of vertical and horizontal wavelengths of all GWs between $37^\circ\text{-}47^\circ\text{S}$ and $47^\circ\text{-}57^\circ\text{S}$ and longitudes between $40^\circ\text{-}90^\circ\text{W}$ at 16 km and 25 km. This indicates ~~at~~ a strong

640 increase in vertical wavelength in the southern part, while the northern part remains almost unchanged. Horizontal wavelengths remain mostly unchanged in both regions. Therefore in the southern part, the GWs refract towards vertical wavelengths larger than the cutoff wavelength of 12 km that is used in the generation of the HIRDLS data set and are thus filtered out at higher altitudes. This finding is confirmed by the unfiltered observation data (without the cutoff at $\lambda_z = 12$ km), which shows a broad maximum at all altitudes (not shown). In addition, the MWM shows more GW activity in the south without the observational
645 filter, which could mean that HIRDLS picks up more of the horizontal spectrum than we assume here-in the observational filter (c.f. Fig. 13)- 13, Trinh et al. (2015)). This strong filtering at higher latitudes is also a likely reason for the relatively weak GWMF predictions of the MWM around the Antarctic Peninsula.

Another major predicted feature is strong GW activity around the Antarctic Peninsula and eastward trailing GWMF, especially at higher altitudes. These predictions agree with observations in terms of extent of the horizontal propagation. The
650 HIRDLS data, however, shows another peculiar pattern: GWMF is increasing again above 20 km altitudealtitude. Since the dataset data set is limited to about 63°S, it is not clear where this is coming from. One source could be orographic waves propagating from further south. This is not seen in the MWM though. Even without the observational filter, there is some northward propagation above the Antarctic Peninsula, but it is far to-too little to compensate the reduction in orographic GWMF with altitude. ~~Therefore, we can attribute this-~~ This feature in the observations might be related to MWs due to katabatic flow (Watanabe
655 et al., 2006) or other, non-orographic processes like spontaneous-imbalances of the polar jet or frontal systems. Partly, this lack of GWMF might also be related to the strong filtering in high latitudes by the observational filter. Note that although GWs excited by katabatic flow are also categorized as MWs, they are not considered by the MWM since they are excited at drops in elevation, which are not detected by the presented algorithm. The eastward propagation seen at 25 km in both data sets is in agreement ~~previous studies of with previous studies by~~ e.g. Sato et al. (2012).

660 Enhanced GW activity is seen in the MWM prediction above the Southern Alps and the Great Dividing Range/Tasmania, which has been shown by Eckermann and Wu (2012) to be a strong MW source. The MWs from Australia and Tasmania show a relatively localized pattern with increasing altitude, while the MWs from the Southern Alps show strong south-eastward propagation especially at higher altitudes. These features are hard to separate from the background in the HIRDLS data and can therefore not be entirely validated. The observation, however, shows some enhanced GWMF around the Southern Alps,
665 which stretches to the southeast and merges with the background at around 170°W. A look into unfiltered MWM data (see Fig. 13) shows that there is strong north-eastward propagation from eastern Antarctica, which can partly explain enhanced fluxes in this region.

Another predicted pattern found in both data sets is enhanced GW activity above the Southern Alps and the Great Dividing Range/Tasmania (a study of this as a MW source has been done by Eckermann and Wu (2012)). The location and strength of
670 local maxima fits-fit nicely between the two. In the observations, these features are of comparable strength as the background and thus difficult to disentangle. At higher altitudes, MW activity from Australia/Tasmania are-is reduced significantly and rather localized. MWs excited by the Southern Alps on the other hand show strong eastward oblique propagation already at 16 km altitude. In the observations, it is not clear whether the long south-eastward trail from New Zealand is caused by MW

propagation or a different GW source, however looking into unfiltered MWM data shows a strong north-eastward propagation
675 of MWs from ~~eastern East~~ Antarctica, which can partly explain enhanced fluxes.

Another predicted feature ~~are MWs~~ is MW activity of similar strength to ~~the ones above~~ New Zealand above South Africa with propagation towards the ~~south-east~~ southeast. This region is usually not regarded as a ~~hot-spot~~ hot spot for GWs, however, we will show that this feature is fairly consistent throughout SH winter in Sect. 5.3. In the satellite data, this feature is obscured by the belt of high GWMF in the Southern Ocean ~~;~~ but could be interpreted as the bend towards the ~~south-east~~ southeast of
680 Africa, ~~that~~ which is seen in this belt.

~~The MWM shows few features in the Northern Hemisphere, although only at 16 km. Above this altitude, MWs encounter a critical level and are filtered out due to the summer wind reversal. Weak GW activity above the northern Rocky mountains, Greenland and the Japanese Sea can be assigned to structurally agreeing counterparts in HIRDLS. Note however that the baseline of HIRDLS is much higher than the predicted GWMF of the MWM and these features might as well not be visible in the observations at all.~~

685

5.2 Zonal mean momentum flux distributions

Figure 12 shows monthly and zonal mean of total GWMF as observed by HIRDLS (a, b) and predicted by the MWM (c – f) for January (left column) and July (right column) 2006. Panels a – d show the height range limited by the HIRDLS data set (14 - 25 km), while panels e and f extend further from 10 - 30 km. The MWM considers only GWMF of orographic origin, while it
690 was shown in Sect. 5.1 that HIRDLS measured high background fluxes all around the globe including all possible GW sources (see Fig. 6 and Fig. 10). In the zonal mean, this leads to rather high values compared to the MWM prediction, which shows gaps above regions, where no MWs are present (e.g. oceans, tropics at high altitude). This leads to the MWM zonal means being of reduced values, which is why the comparison between the data sets is focused on the structural features. The MWM gives information about which patterns in the observations are caused by MWs and which are of other ~~origin~~ origins. Mainly in
695 the tropics, the zonal ~~cross-sections~~ cross-sections show gaps in the ~~HIRDLS~~ HIRDLS data due to clouds and the tropopause seen in Sect. 5.1. ~~Black contour lines~~ While clouds restrict the line of sight of the instrument, data below the tropopause has not been used in the diagnosis of GWMF due to the discontinuity in stability it represents, which could lead to wrongly estimated GW parameters. The black contour lines in Fig. 12 show the monthly mean zonal wind as taken from ERA5 data.

For January 2006, shown in Fig. 12a and c, the same features as in the discussion of Sect. 5.1.1 can be recognized in the zonal
700 mean. A local maximum at around 35°N at low altitudes, which moves northward to about 50°N at 20 km corresponds mainly to the strong GWMF above the Himalaya and Altai mountains and the associated northward shift with increased altitude. The Southern Hemisphere shows most dominantly the southern Andes at around 45°S. Another low altitude maximum at 30°S in the observations is probably not ~~robust~~ representative of the zonal mean, as Fig. 6 shows, that it stems from a very small region with few data points west of Australia. The predicted GWMF is mostly restricted to below the wind reversal, although there is
705 a part of the Andean MWs, that reach up to 25 km at around 40°S. This can be attributed to their horizontal propagation and refraction, to circumvent the ~~wind blocking~~ critical level filtering (also complete ~~wind blocking~~ filtering would require zero meridional wind as well).

Corresponding data for July 2006 is shown in Fig. 12b and d for HIRDLS observations and MWM predictions, respectively. As in Sect. 5.1.2, the dominant feature in both data sets is the GWMF above the southern Andes and the Southern Ocean around 40°-50°S. The prediction from the MWM shows enhanced GWMF around the neck region at roughly 16 km, 30°S. A quick check against the MWM without the observational filter (applied (Fig. 12f) shows that this is most likely not due to (northward) propagation, but due to the shift of MW parameters towards better-observable-values. Below about 20 km, there is also values that are better observable by the instrument, i.e. towards longer vertical wavelengths, and therefore less suppressed after filtering. The observations do not show southward propagation towards 60°S. Observations do not show this explicitly due to the strong band of GWMF obscuring individual features in the zonal mean. The predicted zonal mean does also show no hint of from the MWM, on the other hand, does show neither strong southward propagation from the Southern Andes nor northward propagation of MWs from Antarctica, that which could lead to the enhanced fluxes in the southernmost observations at highest altitudes (about 22–25 km). The model predicts, however, strong northward propagation of meridional momentum flux from the Antarctic Peninsula towards 60°S with decreasing intensity (not shown). As mentioned in Sect. 5.1.2, this feature is therefore enhancement seen in the observations is, therefore, most likely of non-orographic origin and generated by sources higher up in the atmosphere like jet fronts and spontaneous adjustment. In the Northern Hemisphere, the strongest MW activity is seen above 65°N and in the MWM predictions can be attributed to Greenland as a source, followed by MWs excited another local maximum above the Himalaya around 40°N. Both features are confirmed by the observations. The MW activity is well confined by the wind reversal in the summer hemisphere in the simulation, as would be expected for MWs.

In order to discuss the effect of the observational filter, raw MWM data without any filtering applied is shown in Fig. 12e and f for January and July respectively. In general, a reduction of absolute values by a factor of roughly 3 - 10 due to the observational filter can be seen, which depends on the wavelengths and the wave's orientation to the satellite track. Nevertheless, there are also structural changes. For January, the maximum above the Himalaya gets reduced and therefore a net northward shift can be seen. Without the observational filter, there is also an additional feature in the tropics extending quite high. At high latitudes, the Maximum above the Antarctic Peninsula and another smaller one in the Arctic are strongly suppressed by the observational filter. This stronger effect at high latitudes is due to the hard cutoff in vertical wavelength at 12 km in the observational filter. In high latitudes, waves of longer vertical wavelength are more dominant since the intrinsic frequency is usually higher due to being confined to $N^2 > \omega^2 > f^2$. The vertical wave-number-in-mid-frequency-approximation-wavenumber in mid-frequency approximation is given as $|m| = N \frac{|k_{\text{hor}}|}{|\omega|}$, where N is the Brunt-Väisälä frequency and k_{hor} the horizontal wave-number wavenumber. Thus at higher latitudes, where $|f|$ is larger, GWs have in general larger minimal frequencies leading to higher minimal vertical wavelengths.

July shows a very similar picture: the Antarctic Peninsula is strongly suppressed and the maximum between 30°-50°S is reduced in width. Also, the gap at 60°S is increasingly closing at higher altitudes, while the opposite can be seen after application of the observational filter. This gap is closing even more at higher altitudes than shown. Most of the GWMF propagating into this region originates at the Antarctic Peninsula, but also smaller islands like the Falkland Islands, South Georgia and the Kerguelen Islands as well as the southern Andes contribute.

In both cases, the MWM predicts a comparable strong feature just north of the equator, reaching up as high as 20 km in January. Since the observations are limited due to clouds, this is only seen in the model data, ~~but since this feature almost completely vanishes after application of the observational filter, HIRDLS would probably not have observed this.~~ The origin of the MWs is around Thailand/Malaysia and the Philippines. Another feature, that is worth further investigation are MWs crossing the wind blocking critical level filtering (e.g. around 40°S in January). The MWM can be used in an in-depth study, to find the pathways and conditions of these MWs. This is beyond the scope of this model overview study though.

5.3 Time evolution of GWMF distributions

Now we apply the MWM to quantify oblique propagation in more detail and get first insights of a look at GWMF transport patterns. As presented, the model allows to investigate the evolution of MW activity throughout the year and related seasonal patterns. Fig. 13 shows horizontal monthly mean GWMF distributions for January to December 2006 at 25 km altitude. Note however that the observational filter used in Sect. 5.1 was not applied to this data, a comparison to Fig. 6 and Fig. 10 can therefore give an indication of the effect of the observational filter.

At 25 km we expect already strong oblique propagation as this is usually happening in our ray-tracing experiments, the strongest horizontal propagation takes place in a relatively small layer above the tropopause. The summer wind reversal is also below this level. Most MWs in the summer hemisphere are therefore filtered out.

The commonly expected features are evident in the time series: during summer time, MW activity is strongly reduced due to wind filtering at the stratospheric wind reversal. This corresponds to April to September in the northern and December to February in the Southern Hemisphere. In the Northern Hemisphere, however, we see an interesting feature: the MW activity above Asia is suppressed for a longer time period (April to September) than above the Rocky ~~mountains~~ Mountains and in high latitudes (May to approximately August). The reasons behind this could be the position of the wind reversal and might only be a feature special to 2006, which is considered here.

The data shows a band of high GWMF above the northern Atlantic connecting New England to Greenland, Iceland and Europe, which is only interrupted from May to September. The same pattern is visible in HIRDLS observations for January (Fig. 6 a) but was reduced after applying the observational filter to the MWM data.

The total maximum of GWMF throughout the year is located in the Southern Andes and Antarctic Peninsula region, as the current understanding would suggest. There is strong lateral propagation from this region eastward up to the zero meridian, which is in agreement with the findings ~~in~~ of Sato et al. (2012). This zonal propagation and advection was not seen to the same extent in the previous filtered MWM data at 25 km altitude (Fig. 10) due to the rather small strength and specific wave characteristics. The eastward transport of GWMF is an ~~all-year-round~~ all-year-round phenomenon with similar shape in all months though absolute values vary with season and are strongest in austral winter. An interesting finding is additional propagation westward of the Andes, which occurs throughout the year with maximum extent in October and November. This seemingly leeward propagation has been observed by the 2019 SouthTRAC campaign (Rapp et al., 2021) and extensively investigated by Krasauskas et al. (2022).

775 A feature not seen in the filtered data for austral winter (Fig. 10) is a stretched band of GWMF starting at South Africa reaching to the Kerguelen Islands and beyond towards Antarctica. This season in general shows the contribution of smaller oceanic islands, like the Kerguelen, South Georgia, and the Falkland Islands, for generating GW activity at around 60°S and thus slowing down the southern polar vortex in GCMs. These enhanced fluxes above the Kerguelen Islands are also seen in the HIRDLS observations for (austral) autumn months (not shown), while it is overshadowed by the ~~large-scale~~large-scale globe-
780 wrapping GWMF band for July shown in Fig. 10. The distributions agree ~~to~~with the findings of Perrett et al. (2021), which state that GWs above smaller oceanic islands tend to propagate shorter horizontal distances compared to the ones above the Southern Andes and Antarctic Peninsula. The strong MW activity and propagation seen above South Africa is a new finding, that has not been considered before. Due to its persistence for about 4 months, it has a significant impact on the atmosphere.

In general, the MWM predicts strong horizontal propagation all around the globe, especially in the Southern Andes - Drake
785 Passage - Antarctic Peninsula region and New Zealand. But also other parts, that are not as prominently known for it, like the smaller oceanic islands, northern Atlantic and South Africa, should not be neglected. Another point to be made is the similarity and consistency of propagation patterns. For example, if there is strong activity in the Southern Hemisphere, it will be advected towards the west. This might be a general pattern, that approximates a large part of MW propagation throughout the year. Such a simple, flow independent transport pattern could be used for improving MW parameterizations in GCMs.

790 6 Conclusions

In this study, we present a straightforward approach and model for the localization and quantification of orographic gravity wave sources. Using a similar approach as Bacmeister (1993), we use a fit of idealized Gaussian mountain ridges to topographic elevation data for an approximation of the main orographic features able to excite mountain waves. These Gaussian ridges allow for an estimation of the main MW parameters of horizontal wavelength, orientation, and amplitude. We show that our model
795 is able to represent the general ridge structures found in topographic data. Plateaus and largest scale features (which could also lead to MWs by katabatic flow) are not considered in the current state.

Using the ray-tracer GROGRAT (Marks and Eckermann, 1995), we quantify vertical and oblique propagation as well as refraction of excited MWs within the model in time-dependent background atmospheres. Our results show that the MWM is capable of reproducing residual temperature structures comparable to the ~~high-resolution~~high-resolution ECMWF IFS
800 operational analysis. Though the agreement is only qualitative, the ones with expected orographic origin are well reproduced regarding orientation, scale, and amplitude. In particular, ~~smaller-scale~~smaller-scale features agree in location and amplitude between both data sets. Comparisons of global MWM gravity wave momentum flux (GWMF) distributions to corresponding HIRDLS observations between altitudes of 16 - 25 km provide good agreement both in terms of patterns and amplitude (after application of an observational filter to the ~~MWW~~MWM data, accounting for the measurement geometry, see Trinh et al.
805 (2015)). This applies in particular to regions directly above mountainous areas but also to downstream regions, where MWs have propagated ~~to~~ via oblique propagation. The degree of horizontal propagation is compatible with the results of previous studies of Sato et al. (2012). The agreement is therefore adequate for our subsequent ~~MWM-based~~MWM-based analyses.

Investigations of the evolution of MW parameters show that some of the waves refract to very long (Southern Andes) or very short (Himalaya) vertical wavelengths and thus move out of the visibility range of the HIRDLS data set presented here. Refraction leads to a northward shift of the maximum above the Southern Andes and a reduced signal above the Himalaya. In addition, a study of ~~blocking and wind filtering~~ critical level filtering due to the wind profiles shows that GWs ~~in general~~, in general, find better vertical propagation conditions above Mongolia compared to Himalaya. This is associated with a stronger suppression of GW (and MW) activity above the Himalaya.

The wind and propagation conditions above the Rocky ~~mountains~~ Mountains show a complex situation for January 2006. The ~~low level~~ low-level winds are very strong (a factor of 4 stronger than in the Himalaya region) and allow therefore for excitation of strong amplitude MWs. In the lower stratosphere, the excited waves encounter a strong positive vertical ~~gradient~~ in horizontal wind ~~wind shear~~, allowing the amplitude of the waves amplitudes to grow before they reach a strong negative wind shear level above leading up to a wind reversal. In this strong negative shear, high amplitude MWs reach saturation in our model and propagate further at saturation amplitude. However, it would also be possible that they break completely and instead deposit all momentum locally (Kaifler et al., 2015), a process that is currently not captured by the MWM. If this process is physical, the consequence would be that we find an overestimation of GW activity once saturation of these strong MWs sets in. One implication would be that the resulting GW drag will be predicted ~~in at~~ the wrong altitude by the ray-tracer, although it is not certain how much energy of such a breaking wave would be redistributed to other processes ~~like~~, e.g. secondary wave generation.

The interpretation of comparisons of monthly and zonal mean GWMF in the height range of 14-25 km to corresponding HIRDLS data proved to be difficult due to systematic differences between the data sets, like the overlapping signals of non-orographic gravity waves in the observations. Nevertheless, we obtain a good agreement in terms of wave structures for regions of high topographic wave activity. Another finding is that it could be worthwhile to implement katabatic MWs in order to obtain ~~increased fluxes~~ improved GWMF predictions northward of Antarctica and southward of Greenland. MWM predictions for July 2006 without observational filtering show, that the gap at 60°S is closing mainly by MWs propagating from the Antarctic Peninsula towards the Drake Passage, but also from contributions of smaller islands (Falkland Islands, South Georgia, and Kerguelen Islands).

Global monthly mean GWMF distributions throughout the year show that the oblique propagation of MWs is not only a seasonal phenomenon but important during the whole year. Especially MWs excited in the Southern Andes and Antarctic Peninsula propagate strongly for most of the year, both east- and westward. But also in other regions, e.g. in the Northern Atlantic, horizontal relocation of momentum by MWs is important for a large part of the year (about seven months in 2006). This part of our study also underlines the importance of smaller islands around 60°S for the GWMF budget and the need for a better representation of GWs in GCMs.

One of the main goals of this study is the quantification of oblique mountain wave propagation. The results show, that the presented approach is ~~well suited~~ well-suited to shed light on the behavior of MWs and their appearance in observation data (especially since the MWM ~~provide~~ provides access to the parameters of each launched GW). The model might also help in disentangling the influence of primary mountain waves (which are the only waves our model is considering) and waves of other

sources (also secondary waves). Another sign for reasonable representation of oblique propagation is the gap at 60°S closing at higher altitudes, which is partially seen in the zonal mean GWMF comparison of Sect. 5.1 and Sect. 5.2.

845 The results of this study suggest that MWs generated by katabatic flow as well as isotropic mountains (e.g. smaller islands) are worth investigation and inclusion in the MWM for it to capture all possible orographic sources. However, the MWM's performance is good and comparisons of the model's residual temperature to observation campaigns are worthwhile as another tool for explaining the measured GWs path and origin. Thereby the model can be used to separate MWs from non-orographic GWs in observations. Our results support that horizontal propagation of MWs is a strong and global effect that stays important
850 throughout the whole year and is currently not considered in ~~lower-resolution~~ lower-resolution GCMs.

Since there is a good agreement of the wave field characteristics of the MWM to observations and more sophisticated models, it can be used as a predictor for the momentum transport of MWs. In particular, we have shown that there is a more or less general pattern of GWMF redistribution throughout the year, which can be used as a ~~first-order~~ first-order approximation of the horizontal momentum relocation in GCMs. Due to the implementation using a ray-tracer, all necessary information,
855 such as location, momentum, and scales, are covered by the MWM. ~~Implementation~~, which are needed for the estimation of such a ~~pattern-propagation~~ pattern. Implementation of this into a GCM could improve ~~the~~ predictability, especially in the polar vortex region. Böloni et al. (2021) and Kim et al. (2021) have already shown that ray-tracing can be used to improve the representation of subgrid-scale GWs in atmospheric models and that this is a path worth investigating.

Data availability. HIRDLS Level-2 data are available via the NASA Goddard Earth Sciences Data and Information Services Center (GES
860 DISC) at https://acdisc.gesdisc.eosdis.nasa.gov/data/Aura_HIRDLS_Level2/ (NASA GES DISC, 2022)

Code and data availability. Access to the code and data is possible upon request to the authors.

Appendix A: Mountain Wave Model Details

A1 Bandpass filter

The bandpass filter in use in the MWM is based on convolutions with a Gaussian function kernel. Given the ~~small and large~~
865 ~~scale bounds~~ λ_{small} and λ_{large} ~~small- and large-scale bounds~~ λ_{small} and λ_{large} , the corresponding σ , i.e. the width (or standard deviation) of the Gaussian, of the kernels is calculated depending on the grid spacing of the topography (d_x) via:

$$\sigma_i = \frac{\lambda_i}{6d_x}. \quad (\text{A1})$$

In this way, both scales are converted to a pixel scale, which is then used for the smoothing. For the final bandpass filtered topography $H_{bandpass}$ $H_{bandpass}$, we subtract the large scales from the ~~small scale~~ small-scale smoothed field:

$$870 \quad H_{bandpass} = H * G(\sigma_{small}) - H * G(\sigma_{large}). \quad (\text{A2})$$

A2 Mountain ~~wave~~ ridge fit

~~The~~ To find the best-fitting idealized mountain ridge to each ridge candidate detected by the Hough transformation and the corresponding parameters, a least squares fit is performed on a rectangular cutout of the bandpass filtered topography, H_{clip} , around the identified ridge candidate. This cutout is generated by cropping the topography data in a way such that the ridge candidate is oriented horizontally in the center. The length of this cutout is given by the ~~line~~ length of the line segment as given by the Hough transformation, or in other words the length of the ridge candidate, and the width is set to λ_{target} , λ_{large} , which is the upper cutoff of the bandpass filter. ~~The lowest point~~

Since the idealized ridges are of Gaussian shape, i.e. strictly positive, the lowest elevation of the cutout is ~~set~~ shifted to zero via

$$\tilde{H}_{clip} = H_{clip} - \min(H_{clip}). \quad (A3)$$

~~Afterwards, we fit~~ Following this preprocessing, the fit with the idealized ridge, R , to the cutout using the Frobenius (or Euclidean) norm and minimizing the cost function

$$f_{cost} = \frac{1}{\text{size}(\tilde{H}_{clip})} \text{norm} \left(\frac{R - \tilde{H}_{clip}}{\max(\tilde{H}_{clip})} \right).$$

$f(h, a)$, with the parameters height h and width a , is performed by minimizing the least squares difference between the idealized ridge and the cutout of the topography:

$$\underset{h, \sigma}{\text{minimize}} F_{cost} = \sqrt{\sum_{i,j} (f_{ij}(h, a) - \tilde{H}_{clip,ij})^2}. \quad (A4)$$

~~We divide by the maximum of the cutout topography to get the relative error and by the size of it (meaning the number of grid points) to prevent overvaluing small scale ridges~~

Here i and j are the (zonal and meridional) grid indices. This cost function ~~represents thus the mean relative squared deviation of the idealized ridge to the bandpass filtered topography is minimized in terms of the ridge parameters h and a using standard methods, which results in the best-fitting idealized Gaussian mountain ridge for the given topography cutout.~~ The starting values for the optimization are chosen as $h_0 = 100$ m and a_0 corresponding to the center of the considered scale interval.

In principle this ridge could take any shape, here we are using a Gaussian shape as given in Eq. 1.

In addition, if even the optimized parameters result in a bad fit, i.e. a high value of the cost function in Eq. A4, the ridge is disregarded and not considered for the final ridge collection.

Appendix B: The (Probabilistic) Hough Transformation

The ~~here used Hough Transformation and it's~~ Hough transformation used in this study and its probabilistic variant are described in the following. In addition, the sensitivity on parameters and their choice for this study is given.

900 The line detection assumes equidistant grid points and is therefore performed on a local Cartesian grid.

B1 Algorithm and Parameter Choice

The Hough transformation can be interpreted as a discretized version of the Radon transformation, which ~~is widely used in tomography. It aims at representing a~~ allows for de- and reconstruction of multidimensional functions to/from the function values integrated along straight lines (e.g. Herman, 2009). This transformation is the basis of computer tomography. While the
905 Radon transformation is formulated on continuous functions, the Hough transformation acts on discretized fields and is thus better suited for digital image and data processing (Duda and Hart, 1972; Kang et al., 1991).

~~The Hough transformation aims at detecting straight-line structures in 2D image (or images (or a general 2D data in general) by a superposition of (a relatively low number of) straight lines. It set~~ and explicitly relies on the fact that all lines passing through a point $X = (x, y)$ can be described by the parameters (R, θ) , where $R = x \cos(\theta) + y \sin(\theta)$, for $\theta \in [0, \pi)$, with
910 Then R is the line's distance to the origin R and inclination θ . The first step of the Hough transformation is the initialization of an empty accumulator $Hf(R, \theta)$ with discrete $R \in [-r_{max}, r_{max}]$ and $\theta \in [0, \pi)$. The actual size of this matrix depends on the prescribed resolution in θ the inclination of the line w.r.t. the horizontal. The space spanned by R and θ and on $r_{max} = L_x + L_y$, with L_x is also called the Hough space.

The line detection is performed in a "voting" procedure, where every non-zero entry in the data casts votes to all possible
915 lines passing through this data point and thereby increasing the likelihood of these lines being general features in the data set. Technically this is realized by initializing a zero-valued matrix $Hf(R, \theta)$, also called (Hough space) accumulator because it counts the votes, with discrete dimensions $R \in [-r_{max}, r_{max}]$ and L_y being the width and height of the input image. Now, for $\theta \in [0, \pi)$. For each non-zero pixel of the image entry of the data set with coordinates $X_j = (x_j, y_j)$ and each orientation θ_i a value for, a value of $R_{j,i}$ can be calculated. Afterwards, the corresponding point in the Hough space accumulator is calculated
920 for every discrete value of θ_i using the equation above. The corresponding entries in the accumulator matrix, $Hf(R_{j,i}, \theta_i)$ is, are then incremented by one (that pixel in the input image basically gives a 'vote' for all straight lines passing through it). After processing, "voting" for these lines being a feature in the data set. After repeating this process for all non-zero pixels of the image, this will result in local maxima in the accumulator $Hf(r, \theta)$ at exactly those points entries in the initial data set, the accumulator matrix exhibits local maxima exactly at the locations with line parameters (R, θ) that correspond to main line-like
925 straight line structures in the image data set.

The probabilistic Hough transformation improves upon this algorithm ~~by not explicitly processing every possible line through every~~ in a few ways. In the probabilistic version, the non-zero point. Once a single line in the entries are processed in a random order but still "voting" in the same way with votes counted in a Hough space accumulator reaches a given threshold, the corresponding line is scanned along its slope for. However, if at any point a threshold of votes for any line is reached,
930 the data set is tested for the corresponding line feature starting from the last processed data point. This is done by traversing the data set along the corresponding line in both directions in search of further connected points until belonging to the same line segment. If a gap of point of length l_{gap} or the image's border is encountered in either direction. This gives both endpoints of the corresponding line segment and thus fully localizes it within the image. Now, if the traversed line at least length l_{gap} is

935 encountered, where the data set has zero-valued entries, the line traversing in this direction ends. This results in start and end points of the feature in the initial data set and thereby localizes it fully. If this detected feature is longer than a given minimal length l_{min} minimum line length l_{min} , it is accepted and the points making up the line are no longer considered for further iterations. The initial set of points is processed in a probabilistic order, hence the name as a line feature in the data for further processing.

940 The main advantage of the probabilistic algorithm for our use case is the fact, that it results in line segments with defined start and end points which directly give the length, orientation, and position of the line feature.

B2 Sensitivity of the probabilistic Hough Transform

As stated in the main text, the probabilistic Hough transforms capability to detect mountain ridges is highly affected by the minimal line length, l_{min} and the maximal gap along each line, l_{gap} . This is especially true for ease of this work in the consideration of topography data, since natural ridges typically do not form perfect straight lines, but are or squiggle. Thus, this form arcs and/or other more complex structures. This section investigates the sensitivity of the Hough transform on these parameters in the case of the Southern Andes.

To this end, we tested different combinations of l_{min} and l_{gap} and displayed the results l_{min} and l_{gap} . The corresponding results are displayed in Fig. B1, where the maximum line gap, l_{gap} , varies with column from 10 km to 50 km and the minimum line length, l_{min} , varies with row from 30 km to 120 km. For small l_{min} and l_{gap} (Fig. B1 b)), the a), most structures are well covered by detected line segments. However, these lines are in general very short and thus would not correspond to ideal necessarily correspond to 2D-like mountain ridges. For higher l_{min} in combination with a small l_{gap} (B1 e) l_{gap} (e.g. Fig. B1 g, k), only the straightest very straight structures are detected, which gives good candidates for ideal long stretched mountain ridges, long-stretched mountain ridges but neglects possible smaller scale ones. A too small l_{gap} smaller-scale ones. The allowed gap in these line segments is too short to account for any bends in the underlying structures. A small l_{gap} combined with a high l_{min} very high l_{min} (Fig. B1 e)j) is highly restrictive, and does no good job in describing the general patterns. A higher l_{gap} and does detect barely any line segment in the complex topography skeleton. A high l_{gap} (Fig. B1 c), f) on the other hand leads to artifacts crossing large gaps between true structures line segments spanning in between parallel line structures, where there is no underlying support in either the skeleton or the topography.

960 Since there is a need to also detect natural curved and non-perfect straight mountain ridges, one needs to balance both parameters. There is certainly a trade-off trade-off, if one wants to detect mountain ridges of arbitrary length with a single set of l_{min} and l_{gap} l_{min} and l_{gap} .

We found that $l_{min} = 60$ km and $l_{gap} = 30$ km (shown in Fig. B1 e) results in a reasonable trade-off for both parameters. With a minimal line length of 60 km most of the features are detectable within the scale ranges that we are interested in. This choice of parameters is used for all results in the present study.

965 Appendix C: Alternative representation of ridges as used in previous studies Topography approximation

The here presented mountain wave model is inspired by the study in Baemeister (1993) and Baemeister et al. (1994). To compare it to these previous mountain wave modeling studies, we have recreated similar plots to their representation of mountain ridges. For this we approximate each mountain ridge with a rectangular box. This section gives more detail on the performance of reconstructing the topography from the fitted ridges. First additional information on the Southern Andes case is provided to give a better overview of how each single spectral band is detected from the topography. Following this is the approximation by ridges of the Himalaya and southern Africa region, which are mentioned explicitly in the text.

C1 Southern Andes ridge finding

The ridge-finding algorithm operates on scale intervals and detects the ridges in the bandpass filtered topography data. This is illustrated in Fig. C1, where the rectangles width is given by half the estimated wavelength and its length is taken as the length of topography after application of the bandpass filter is shown in the left column and the underlying ridge. As in the mentioned previous studies, we draw these rectangles atop of each other in order of ascending ridge height. This reconstruction, which is better comparable to the studies in Baemeister et al. (1994); Eckermann et al. (2000); Kruse et al. (2021), is shown corresponding reconstruction of detected ridges in the right column. Note that each spectral band was reconstructed by taking the maximum of all ridges that cover the same spot. The four largest scale intervals given in Table 1 yielded no ridges in this region and are therefore not shown.

Figure C1 shows that each individual contribution to the full spectrum of elevation features in the original elevation data is detected and reconstructed in a good way. Features agree in orientation height and length.

C2 Himalaya and southern Africa

The same topography reconstruction separated in small- and large-scale contributions as in Fig. ?? for North America including the dominant Rocky Mountain region and 2 for the Mongolia region and southern Africa are shown in Fig. ??-C2. Similar comments as for the Southern Andes area, which was considered oftentimes in the present study. Note that the scale of the plots shows only the height of the singular drawn ridge and not the accumulated orographic height of all ridges combined as in Fig. 2 and Rocky Mountain region are applicable here. The very large-scale plateaus, especially the Tibetan Plateau as a whole, are not described due to the limitation in terms of horizontal scales. small-scale features, on the other hand, are approximated well in terms of orientation and location. The total height for the larger, i.e. 200 km and above, scales are, as for the Rocky Mountains region, over-represented due to multiple ridges contributing to the same feature in different directions.

Appendix D: Amplitude correction due to horizontal dispersion

The amplitude calculation in GROGRAT neglects contributions from the last term in Eq. 6. This might, however, lead to deviations for dispersing wave packets. Therefore, we estimated the contribution of this term locally according to

$$995 \quad \underbrace{c_{g,z} \nabla \cdot \mathbf{j}} = c_{g,z} \left(\underbrace{\partial_x \frac{c_{g,x}}{c_{g,z}} + \partial_y \frac{c_{g,y}}{c_{g,z}}}_{\phantom{c_{g,z} \nabla \cdot \mathbf{j}}}, \quad (D1)$$

where the analytical expressions for $c_{g,i}$ were taken from Marks and Eckermann (1995). This gives a local approximation of the change in the horizontal extent of the wave packet along the ray path.

1000 The GWMF experiments for June and July 2006 in comparison to the unmodified GROGRAT amplitudes are shown in Fig. D1 and Fig. D2, respectively. To both, the observational filter of HIRDLS has been applied. In direct comparison, we see that the general amplitude above strong orography is mostly unchanged by the modification. On the other hand, regions, where GWs propagate to are enhanced by this modification. This is as expected, since the term in Eq. D1 is related to the horizontal dispersion of the GW, which is stronger for refracting and turning waves. GWs that propagate far from their sources are more likely to encounter differing wind conditions and thereby refract or turn. The local approximation of this effect is, however, not a replacement for ray tube techniques describing the GW extent in phase space (e.g. Muraschko et al., 2015).

1005 *Author contributions.* SR and PP conceptualized the study, ME performed HIRDLS processing and analysis, SR conceptualized and developed the MWM and performed the simulations. PP and MR supervised the study and JU acquired the funding. SR wrote the manuscript. All authors provided scientific input and reviewed the manuscript.

Competing interests. We, the authors, declare that there are no competing interests present.

1010 *Acknowledgements.* The work of SR was funded by the German Research Foundation (Deutsche Forschungsgemeinschaft, DFG) project UN 311/4-1. In addition, SR and his visit to JB was partly funded by DFG project PR 919/5-1. The work of LK was partly funded by the [Federal German Ministry for Education and Research under grant 01-LG-1907 \(Bundesministerium für Bildung und Forschung, BMBF\) under grant 01LG1907](#) (project WASCLIM) in the frame of the Role of the Middle Atmosphere in Climate (ROMIC)-program. The work of ME was supported by the German Research Foundation (Deutsche Forschungsgemeinschaft, DFG) project ER 474/4-2 (MS-GWaves/SV), which is part of the DFG research unit FOR 1898 (MS-GWaves). The work by ME was also supported by the Federal German Ministry for Education and Research (Bundesministerium für Bildung und Forschung, BMBF) project QUBICC (grant no. 01LG1905C), which is part of the Role of the Middle Atmosphere in Climate II (ROMIC-II) program of BMBF.

References

- Albers, J. R. and Birner, T.: Vortex Preconditioning due to Planetary and Gravity Waves prior to Sudden Stratospheric Warmings, *J. Atmos. Sci.*, 71, 4028–4054, <https://doi.org/10.1175/JAS-D-14-0026.1>, 2014.
- 1020 Alexander, M. J. and Dunkerton, T. J.: A spectral parameterization of mean-flow forcing due to breaking gravity waves, *J. Atmos. Sci.*, 56, 4167–4182, 1999.
- Alexander, M. J., Eckermann, S. D., Broutman, D., and Ma, J.: Momentum flux estimates for South Georgia Island mountain waves in the stratosphere observed via satellite, *Geophys. Res. Lett.*, 36, <https://doi.org/10.1029/2009GL038587>, 2009.
- Alexander, M. J., Geller, M., McLandress, C., Polavarapu, S., Preusse, P., Sassi, F., Sato, K., Eckermann, S., Ern, M., Hertzog, A., Kawatani, Y., Pulido, M., Shaw, T. A., Sigmond, M., Vincent, R., and Watanabe, S.: Recent developments in gravity-wave effects in climate models and the global distribution of gravity-wave momentum flux from observations and models, *Quart. J. Roy. Meteorol. Soc.*, 136, 1103–1124, <https://doi.org/10.1002/qj.637>, 2010.
- 1025 Alexander, S. P., Sato, K., Watanabe, S., Kawatani, Y., and Murphy, D. J.: Southern Hemisphere Extratropical Gravity Wave Sources and Intermittency Revealed by a Middle-Atmosphere General Circulation Model, *Journal of the Atmospheric Sciences*, 73, 1335 – 1349, <https://doi.org/https://doi.org/10.1175/JAS-D-15-0149.1>, 2016.
- 1030 Amante, C. and Eakins, B.: ETOPO1 1 Arc-Minute Global Relief Model: Procedures, Data Sources and Analysis, <https://doi.org/10.7289/V5C8276M>, last access: 20 February 2020, 2009.
- Andrews, D. G., Holton, J. R., and Leovy, C. B.: *Middle Atmosphere Dynamics*, vol. 40 of *International Geophysics Series*, Academic Press, 1987.
- 1035 Aviación Global: Flying across the Andes. Mountain wave., <http://www.aviacionglobal.com/miscellaneous/flying-across-the-andes-mountain-wave/>, last accessed on 31.05.22, 2019.
- Bacmeister, J., Newman, P., Gary, B., and Chan, K.: An algorithm for forecasting mountain wave-related turbulence in the stratosphere, *Wea. Forecast.*, 9, 241–253, [https://doi.org/10.1175/1520-0434\(1994\)009<0241:AAFFMW>2.0.CO;2](https://doi.org/10.1175/1520-0434(1994)009<0241:AAFFMW>2.0.CO;2), 1994.
- Bacmeister, J. T.: Mountain-wave drag in the stratosphere and mesosphere inferred from observed winds and a simple mountain-wave parameterization scheme, *J. Atmos. Sci.*, 50, 377–399, 1993.
- 1040 Barry, R. G.: *Mountain Weather and Climate*, ISBN 978-0511754753, Cambridge University Press, Cambridge, UK, third edn., <https://doi.org/10.1017/CBO9780511754753>, 2008.
- Boldmethod: The Hidden Dangers Of Mountain Wave, <https://www.boldmethod.com/learn-to-fly/weather/how-mountain-wave-forms-and-the-dangers-it-can-create/>, last accessed on 31.05.22, 2016.
- 1045 Butchart, N., Charlton-Perez, A. J., Cionni, I., Hardiman, S. C., Haynes, P. H., Krueger, K., Kushner, P. J., Newman, P. A., Osprey, S. M., Perlwitz, J., Sigmond, M., Wang, L., Akiyoshi, H., Austin, J., Bekki, S., Baumgaertner, A., Braesicke, P., Bruehl, C., Chipperfield, M., Dameris, M., Dhomse, S., Eyring, V., Garcia, R., Garny, H., Joeckel, P., Lamarque, J.-F., Marchand, M., Michou, M., Morgenstern, O., Nakamura, T., Pawson, S., Plummer, D., Pyle, J., Rozanov, E., Scinocca, J., Shepherd, T. G., Shibata, K., Smale, D., Teyssedre, H., Tian, W., Waugh, D., and Yamashita, Y.: Multimodel climate and variability of the stratosphere, *J. Geophys. Res. Atmos.*, 116, <https://doi.org/10.1029/2010JD014995>, 2011.
- 1050 Bölöni, G., Kim, Y.-H., Borchert, S., and Achatz, U.: Toward Transient Subgrid-Scale Gravity Wave Representation in Atmospheric Models. Part I: Propagation Model Including Nondissipative Wave–Mean-Flow Interactions, *Journal of the Atmospheric Sciences*, 78, 1317 – 1338, <https://doi.org/https://doi.org/10.1175/JAS-D-20-0065.1>, 2021.

- C3S, C. C. C. S.: ERA5: Fifth generation of ECMWF atmospheric reanalyses of the global climate., <https://cds.climate.copernicus.eu/cdsapp#!/home>, 2017.
- Center, N. N. G. D.: ETOPO1 1 Arc-Minute Global Relief Model, <https://www.ngdc.noaa.gov/mgg/global/>, last access: 21 June 2021, 2009.
- Chane-Ming, F., Molinaro, F., Leveau, J., Keckhut, P., Hauchecorne, A., and Godin, S.: Vertical short-scale structures in the upper tropospheric and lower stratospheric temperature and ozone at la Réunion Island (20.8°S 55.3°E), *Journal of Geophysical Research: Atmospheres*, 105, 26 857–26 870, <https://doi.org/https://doi.org/10.1029/2000JD900199>, 2000.
- 1060 Choi, H.-J. and Chun, H.-Y.: Momentum Flux Spectrum of Convective Gravity Waves. Part I: An Update of a Parameterization Using Mesoscale Simulations, *J. Atmos. Sci.*, 68, 739–759, <https://doi.org/10.1175/2010JAS3552.1>, 2011.
- de la Camara, A. and Lott, F.: A parameterization of gravity waves emitted by fronts and jets, *GEOPHYSICAL RESEARCH LETTERS*, 42, 2071–2078, <https://doi.org/10.1002/2015GL063298>, 2015.
- Duda, R. O. and Hart, P. E.: Use of the Hough transformation to detect lines and curves in pictures, *Communications of the ACM*, 15, 11–15, 1065 1972.
- Eckermann, S. D. and Marks, C. J.: GROGRAT: a New Model of the Global propagation and Dissipation of Atmospheric Gravity Waves, *Adv. Space Res.*, 20, 1253–1256, 1997.
- Eckermann, S. D. and Preusse, P.: Global measurements of stratospheric mountain waves from space, *Science*, 286, 1534–1537, <https://doi.org/10.1126/science.286.5444.1534>, 1999.
- 1070 Eckermann, S. D. and Wu, D. L.: Satellite detection of orographic gravity-wave activity in the winter subtropical stratosphere over Australia and Africa, *Geophys. Res. Lett.*, 39, <https://doi.org/https://doi.org/10.1029/2012GL053791>, 2012.
- Eckermann, S. D., Broutman, D., Tan, K. A., Preusse, P., and Bacmeister, J. T.: Mountain Waves in the Stratosphere, *NRL-Review*, pp. 73–84, 2000.
- Ehard, B., Kaifler, B., Kaifler, N., and Rapp, M.: Evaluation of methods for gravity wave extraction from middle-atmospheric lidar temperature measurements, *Atmos. Meas. Tech.*, 8, 4645–4655, <https://doi.org/10.5194/amt-8-4645-2015>, 2015.
- 1075 Ehard, B., Kaifler, B., Dörnbrack, A., Preusse, P., Eckermann, S., Bramberger, M., Gisinger, S., Kaifler, N., Liley, B., Wagner, J., and Rapp, M.: Horizontal propagation of large amplitude mountain waves in the vicinity of the polar night jet, *J. Geophys. Res. Atmos.*, pp. 1423–1436, <https://doi.org/10.1002/2016JD025621>, 2016JD025621, 2017.
- Ern, M., Preusse, P., Alexander, M. J., and Warner, C. D.: Absolute values of gravity wave momentum flux derived from satellite data, *J. Geophys. Res. Atmos.*, 109, <https://doi.org/10.1029/2004JD004752>, 2004.
- 1080 Ern, M., Trinh, Q. T., Preusse, P., Gille, J. C., Mlynczak, M. G., Russell III, J. M., and Riese, M.: GRACILE: A comprehensive climatology of atmospheric gravity wave parameters based on satellite limb soundings, *Earth Syst. Sci. Dat.*, 10, 857–892, <https://doi.org/10.5194/essd-10-857-2018>, 2018.
- Ern, M., Trinh, Q. T., Kaufmann, M., Krisch, I., Preusse, P., Ungermann, J., Zhu, Y., Gille, J. C., Mlynczak, M. G., Russell, III, J. M., Schwartz, M. J., and Riese, M.: Satellite observations of middle atmosphere gravity wave absolute momentum flux and of its vertical gradient during recent stratospheric warmings, *Atmos. Chem. Phys.*, 16, 9983–10 019, <https://doi.org/10.5194/acp-16-9983-2016>, 2016.
- 1085 Ern, M., Hoffmann, L., Rhode, S., and Preusse, P.: The mesoscale gravity wave response to the 2022 Tonga volcanic eruption: AIRS and MLS satellite observations and source backtracing, *Geophys. Res. Lett.*, 49, <https://doi.org/10.1029/2022GL098626>, 2022.
- Fritts, D. and Alexander, M.: Gravity wave dynamics and effects in the middle atmosphere, *Rev. Geophys.*, 41, 1090 <https://doi.org/10.1029/2001RG000106>, 2003.
- Fritts, D. C.: Gravity wave saturation in the middle atmosphere: A review of theory and observations, *Rev. Geophys.*, 22, 275–308, 1984.

- Fritts, D. C. and Rastogi, P. K.: Convective and dynamical instabilities due to gravity wave motions in the lower and middle atmosphere: theory and observations, *Radio Sci.*, 20, 1247–1277, 1985.
- 1095 Garcia, R. R., Smith, A. K., Kinnison, D. E., de la Camara, A., and Murphy, D. J.: Modification of the Gravity Wave Parameterization in the Whole Atmosphere Community Climate Model: Motivation and Results, *J. Atmos. Sci.*, 74, 275–291, <https://doi.org/10.1175/JAS-D-16-0104.1>, 2017.
- Garfinkel, C. I. and Oman, L. D.: Effect of Gravity Waves From Small Islands in the Southern Ocean on the Southern Hemisphere Atmospheric Circulation, *Journal of Geophysical Research: Atmospheres*, 123, 1552–1561, <https://doi.org/https://doi.org/10.1002/2017JD027576>, 2018.
- 1100 Geldenhuys, M., Preusse, P., Krisch, I., Zülicke, C., Ungermann, J., Ern, M., Friedl-Vallon, F., and Riese, M.: Orographically induced spontaneous imbalance within the jet causing a large-scale gravity wave event, *Atmos. Chem. Phys.*, <https://doi.org/10.5194/acp-21-10393-2021>, 2021.
- Geller, M. A., Alexander, M. J., Love, P. T., Bacmeister, J., Ern, M., Hertzog, A., Manzini, E., Preusse, P., Sato, K., Scaife, A. A., and Zhou, T.: A comparison between gravity wave momentum fluxes in observations and climate models, *J. Clim.*, 26, 6383–6405, 1105 <https://doi.org/10.1175/JCLI-D-12-00545.1>, 2013.
- Gille, J. C., Barnett, J. J., Whitney, J. G., Dials, M. A., Woodard, D., Rudolf, W. P., Lambert, A., and Mankin, W.: The High-Resolution Dynamics Limb Sounder (HIRDLs) experiment on AURA, *Proc. SPIE*, 5152, 161–171, <https://doi.org/10.1117/12.507657>, 2003.
- Guarino, M.-V., Teixeira, M. A. C., Keller, T. L., and Sharman, R. D.: Mountain-Wave Turbulence in the Presence of Directional Wind Shear over the Rocky Mountains, *Journal of the Atmospheric Sciences*, 75, 1285 – 1305, <https://doi.org/10.1175/JAS-D-17-0128.1>, 2018.
- 1110 Hasha, A., Bühler, O., and Scinocca, J.: Gravity wave refraction by three-dimensionally varying winds and the global transport of angular momentum, *J. Atmos. Sci.*, 65, 2892–2906, 2008.
- Herman, G.: *Fundamentals of Computerized Tomography: Image Reconstruction from Projections*, *Advances in Computer Vision and Pattern Recognition*, Springer London, <https://books.google.de/books?id=hF68xAEACAAJ>, 2009.
- Hersbach, H., Bell, B., Berrisford, P., Hirahara, S., Horanyi, A., Muñoz-Sabater, J., Nicolas, J., Peubey, C., Radu, R., Schepers, D., Simmons, 1115 A., Soci, C., Abdalla, S., Abellan, X., Balsamo, G., Bechtold, P., Biavati, G., Bidlot, J., Bonavita, M., De Chiara, G., Dahlgren, P., Dee, D., Diamantakis, M., Dragani, R., Flemming, J., Forbes, R., Fuentes, M., Geer, A., Haimberger, L., Healy, S., Hogan, R. J., Holm, E., Janiskova, M., Keeley, S., Laloyaux, P., Lopez, P., Lupu, C., Radnoti, G., de Rosnay, P., Rozum, I., Vamborg, F., Villaume, S., and Thepaut, J.-N.: The ERA5 global reanalysis, *Quart. J. Roy. Meteorol. Soc.*, 146, 1999–2049, <https://doi.org/10.1002/qj.3803>, 2020.
- Hertzog, A., Souprayen, C., and Hauchecorne, A.: Eikonal simulations for the formation and the maintenance of atmospheric gravity wave 1120 spectra, *Journal of Geophysical Research: Atmospheres*, 107, ACL 4–1–ACL 4–14, <https://doi.org/https://doi.org/10.1029/2001JD000815>, 2002.
- Hindley, N. P., Wright, C. J., Gadian, A. M., Hoffmann, L., Hughes, J. K., Jackson, D. R., King, J. C., Mitchell, N. J., Moffat-Griffin, T., Moss, A. C., Vosper, S. B., and Ross, A. N.: Stratospheric gravity waves over the mountainous island of South Georgia: testing a high-resolution dynamical model with 3-D satellite observations and radiosondes, *Atmospheric Chemistry and Physics*, 21, 7695–7722, 1125 <https://doi.org/10.5194/acp-21-7695-2021>, 2021.
- Hindley, N. P., Wright, C. J., Hoffmann, L., Moffat-Griffin, T., and Mitchell, N. J.: An 18-year climatology of directional stratospheric gravity wave momentum flux from 3-D satellite observations, *Geophys. Res. Lett.*, 47, e2020GL089 557, <https://doi.org/10.1029/2020GL089557>, 2020.

- Hines, C.: INTERNAL ATMOSPHERIC GRAVITY WAVES AT IONOSPHERIC HEIGHTS, *Canadian Journal of Physics*, 38, 1441–1481, <https://doi.org/10.1139/p60-150>, 1960.
- 1130 Hocking, W.: The Effects of Middle Atmosphere Turbulence on Coupling between Atmospheric Regions, *Journal of geomagnetism and geoelectricity*, 43, 621–636, https://doi.org/10.5636/jgg.43.Supplement2_621, 1991.
- Holton, J. R.: The Influence of Gravity Wave Breaking on the General Circulation of the Middle Atmosphere, *J. Atmos. Sci.*, 40, 2497–2507, [https://doi.org/10.1175/1520-0469\(1983\)040<2497:TIOGWB>2.0.CO;2](https://doi.org/10.1175/1520-0469(1983)040<2497:TIOGWB>2.0.CO;2), 1983.
- 1135 Jähne, B., Scharf, H., and Körkel, S.: Principles of Filter Design, in: *Handbook of computer vision and applications*, edited by Jähne, B., Haußecker, H., and Geißler, P., vol. 2, pp. 125–151, Academic Press, 1999.
- Jiang, J., Eckermann, S., Wu, D., and Ma, J.: A search for mountain waves in MLS stratospheric limb radiances from the winter Northern Hemisphere: Data analysis and global mountain wave modeling, *J. Geophys. Res. Atmos.*, 109, <https://doi.org/10.1029/2003JD003974>, 2004.
- 1140 Jiang, J. H., Wu, D. L., and Eckermann, S. D.: Upper Atmosphere Research Satellite (UARS) MLS observations of mountain waves over the Andes, *J. Geophys. Res.*, 107, 8273, <https://doi.org/10.1029/2002JD002091>, 2002.
- Jiang, J. H., Su, H., Zhai, C., Perun, V. S., Del Genio, A., Nazarenko, L. S., Donner, L. J., Horowitz, L., Seman, C., Cole, J., Gettelman, A., Ringer, M. A., Rotstayn, L., Jeffrey, S., Wu, T., Brient, F., Dufresne, J.-L., Kawai, H., Koshiro, T., Watanabe, M., L'Écuyer, T. S., Volodin, E. M., Iversen, T., Drange, H., Mesquita, M. D. S., Read, W. G., Waters, J. W., Tian, B., Teixeira, J., and Stephens, G. L.: Evaluation of cloud and water vapor simulations in CMIP5 climate models using NASA “A-Train” satellite observations, *J. Geophys. Res.*, 117, n/a–n/a, <https://doi.org/10.1029/2011JD017237>, 2012.
- 1145 Kaifler, B., Kaifler, N., Ehard, B., Doernbrack, A., Rapp, M., and Fritts, D. C.: Influences of source conditions on mountain wave penetration into the stratosphere and mesosphere, *Geophys. Res. Lett.*, 42, 9488–9494, <https://doi.org/10.1002/2015GL066465>, 2015.
- Kang, C.-W., Park, R.-H., and Lee, K.-H.: Extraction of straight line segments using rotation transformation: generalized hough transformation, *Pattern Recognition*, 24, 633–641, [https://doi.org/https://doi.org/10.1016/0031-3203\(91\)90030-9](https://doi.org/https://doi.org/10.1016/0031-3203(91)90030-9), 1991.
- 1150 Kidston, J., Scaife, A. A., Hardiman, S. C., Mitchell, D. M., Butchart, N., Baldwin, M. P., and Gray, L. J.: Stratospheric influence on tropospheric jet streams, storm tracks and surface weather, *Nature Geosci.*, 8, 433–440, <https://doi.org/10.1038/ngeo2424>, 2015.
- Kim, Y.-H., Bölöni, G., Borchert, S., Chun, H.-Y., and Achatz, U.: Toward Transient Subgrid-Scale Gravity Wave Representation in Atmospheric Models. Part II: Wave Intermittency Simulated with Convective Sources, *Journal of the Atmospheric Sciences*, 78, 1339 – 1357, <https://doi.org/https://doi.org/10.1175/JAS-D-20-0066.1>, 2021.
- 1155 Kim, Y.-J., Eckermann, S. D., and Chun, H.-Y.: An overview of the past, present and future of gravity-wave drag parameterization for numerical climate and weather prediction models, *Atmosphere-Ocean*, 41, 65–98, 2003.
- Krasauskas, L., Kaifler, B., Rhode, S., Ungermann, J., Woiwode, W., and Preusse, P.: Oblique propagation of mountain waves to the upwind side of the Andes observed by GLORIA and ALIMA during the SouthTRAC campaign, *Earth and Space Science Open Archive*, p. 37, <https://doi.org/10.1002/essoar.10512325.1>, 2022.
- 1160 Krisch, I., Preusse, P., Ungermann, J., Dörnbrack, A., Eckermann, S. D., Ern, M., Friedl-Vallon, F., Kaufmann, M., Oelhaf, H., Rapp, M., Strube, C., and Riese, M.: First tomographic observations of gravity waves by the infrared limb imager GLORIA, *Atmos. Chem. Phys.*, 17, 14 937–14 953, <https://doi.org/10.5194/acp-17-14937-2017>, 2017.
- Kruse, C. G., Alexander, M. J., Hoffmann, L., van Niekerk, A., Polichtchouk, I., Bacmeister, J., Holt, L., Plougonven, R., Sacha, P., Wright, C., Sato, K., Shibuya, R., Gisinger, S., Ern, M., Meyer, C., , and Stein, O.: Observed and Modeled Mountain Waves from the Surface to
- 1165

- the Mesosphere near the Drake Passage, *Journal of the Atmospheric Sciences*, 79, 909 – 932, <https://doi.org/10.1175/JAS-D-21-0252.1>, 2022.
- 1170 Kruse, C. G., Alexander, M. J., Hoffmann, L., van Niekerk, A., Polichtchouk, I., Bacmeister, J., Holt, L., Plougonven, R., Sacha, P., Wright, C., Sato, K., Shibuya, R., Gisinger, S., Ern, M., Meyer, C., , and Stein, O.: Observed and modeled mountain waves from the surface to the mesosphere near the Drake Passage, *J. Atmos. Sci.*, p. submitted, 2021.
- Lighthill, M. J.: *Waves in Fluids*, Cambridge University Press, p. 504pp, 1978.
- Lott, F. and Miller, M. J.: A new subgrid scale orographic drag parameterization: Its formulation and testing, *Quart. J. Roy. Meteorol. Soc.*, 123, 101–127, 1997.
- 1175 Marks, C. J. and Eckermann, S. D.: A Three-Dimensional Nonhydrostatic Ray-Tracing Model for Gravity Waves: Formulation and Preliminary Results for the Middle Atmosphere, *J. Atmos. Sci.*, 52, 1959–1984, [https://doi.org/10.1175/1520-0469\(1995\)052<1959:ATDNRT>2.0.CO;2](https://doi.org/10.1175/1520-0469(1995)052<1959:ATDNRT>2.0.CO;2), 1995.
- McIntyre, M. E.: Breaking waves and global scale chemical transport in the Earth’s atmosphere, with spinoffs for the Sun’s interior, *Prog. of Theor. Phys. / Suppl.*, 130, 137–166, 1998.
- 1180 McLandress, C., Shepherd, T. G., Polavarapu, S., and Beagley, S. R.: Is Missing Orographic Gravity Wave Drag near 60 degrees S the Cause of the Stratospheric Zonal Wind Biases in Chemistry Climate Models?, *J. Atmos. Sci.*, 69, 802–818, <https://doi.org/10.1175/JAS-D-11-0159.1>, 2012.
- Muraschko, J., Fruman, M. D., Achatz, U., Hickel, S., and Toledo, Y.: On the application of Wentzel-Kramer-Brillouin theory for the simulation of the weakly nonlinear dynamics of gravity waves (vol 141, pg 3446, 2015), *Quart. J. Roy. Meteorol. Soc.*, 141, 3446, <https://doi.org/10.1002/qj.2719>, 2015.
- 1185 Nappo, C. J.: *An Introduction to Atmospheric Gravity Waves*, ISBN 978-0-12-385223-6, Academic Press, second edn., 2012.
- NASA Goddard Earth Sciences Data and Information Services Center: NASA GES DISC: The HIRDLS Level 2 product [data set], https://acdisc.gesdisc.eosdis.nasa.gov/data/Aura_HIRDLS_Level2/, last accessed on 19 October 2022.
- Perrett, J. A., Wright, C. J., Hindley, N. P., Hoffmann, L., Mitchell, N. J., Preusse, P., Strube, C., and Eckermann, S. D.: Determining gravity wave sources and propagation in the southern hemisphere by ray-tracing AIRS measurements, *Geophys. Res. Lett.*, 48, e2020GL088 621, <https://doi.org/10.1029/2020GL088621>, 2021.
- 1190 Pitteway, M. L. V. and Hines, C. O.: The viscous damping of atmospheric gravity waves, *Canadian Journal of Physics*, 41, 1935–1948, <https://doi.org/10.1139/p63-194>, 1963.
- Polichtchouk, I., Shepherd, T. G., Hogan, R. J., and Bechtold, P.: Sensitivity of the Brewer-Dobson Circulation and Polar Vortex Variability to Parameterized Nonorographic Gravity Wave Drag in a High-Resolution Atmospheric Model, *J. Atmos. Sci.*, 75, 1525–1543, <https://doi.org/10.1175/JAS-D-17-0304.1>, 2018.
- 1195 Preusse, P., Eidmann, G., Eckermann, S. D., Schaeler, B., Spang, R., and Offermann, D.: Indications of convectively generated gravity waves in CRISTA temperatures, *Adv. Space Res.*, 27, 1653–1658, 2001.
- Preusse, P., Dörnbrack, A., Eckermann, S. D., Riese, M., Schaeler, B., Bacmeister, J. T., Broutman, D., and Grossmann, K. U.: Space-based measurements of stratospheric mountain waves by CRISTA, 1. Sensitivity, analysis method, and a case study, *J. Geophys. Res.*, 107(D23), <https://doi.org/10.1029/2001JD000699>, 2002.
- 1200 Preusse, P., Ern, M., Bechtold, P., Eckermann, S. D., Kalisch, S., Trinh, Q. T., and Riese, M.: Characteristics of gravity waves resolved by ECMWF, *Atmos. Chem. Phys.*, 14, 10 483–10 508, <https://doi.org/10.5194/acp-14-10483-2014>, 2014.

- Rapp, M., Kaifler, B., Dörnbrack, A., Gisinger, S., Mixa, T., Reichert, R., Kaifler, N., Knobloch, S., Eckert, R., Wildmann, N., Giez, A., Krasauskas, L., Preusse, P., Geldenhuys, M., Riese, M., Woiwode, W., Friedl-Vallon, F., Sinnhuber, B.-M., de la Torre, A., Alexander, P., Hormaechea, J. L., Janches, D., Garhammer, M., Chau, J. L., Conte, J. F., Hoor, P., and Engel, A.: SOUTHTRAC-GW: An Airborne Field Campaign to Explore Gravity Wave Dynamics at the World's Strongest Hotspot, *Bull. Amer. Meteor. Soc.*, 102, E871 – E893, <https://doi.org/10.1175/BAMS-D-20-0034.1>, 2021.
- 1205 Saha, S., Niranjan Kumar, K., Sharma, S., Kumar, P., and Joshi, V.: Can Quasi-Periodic Gravity Waves Influence the Shape of Ice Crystals in Cirrus Clouds?, *Geophysical Research Letters*, 47, e2020GL087909, <https://doi.org/https://doi.org/10.1029/2020GL087909>, e2020GL087909 2020GL087909, 2020.
- 1210 Salby, M. L. and Callaghan, P.: Sampling Error in Climate Properties Derived from Satellite Measurements: Consequences of Undersampled Diurnal Variability, *Journal of Climate*, 10, 18 – 36, [https://doi.org/10.1175/1520-0442\(1997\)010<0018:SEICPD>2.0.CO;2](https://doi.org/10.1175/1520-0442(1997)010<0018:SEICPD>2.0.CO;2), 1997.
- Salby, M. L. and Garcia, R. R.: Transient response to localized episodic heating in the tropics. Part I: Excitation and short-time near-field behavior, *J. Atmos. Sci.*, 44, 458–498, 1987.
- 1215 Sato, K., Tateno, S., Watanabe, S., and Kawatani: Gravity wave characteristics in the Southern Hemisphere revealed by a high-resolution middle-atmosphere general circulation model, *J. Atmos. Sci.*, 69, 1378–1396, <https://doi.org/10.1175/JAS-D-11-0101.1>, 2012.
- Shepherd, T. G.: Atmospheric circulation as a source of uncertainty in climate change projections, *Nature Geosci.*, 7, 703–708, <https://doi.org/10.1038/NNGEO2253>, 2014.
- Skamarock, W. C.: Evaluating mesoscale NWP models using kinetic energy spectra, *Mon. Weath. Rev.*, 132, 3019–3032, 2004.
- 1220 Smithsonian Magazine: The Calculators of Calm, <https://www.smithsonianmag.com/air-space-magazine/the-calculators-of-calm-7629296/>, last accessed on 31.05.22, 2005.
- Song, B.-G., Chun, H.-Y., and Song, I.-S.: Role of gravity waves in a vortex-split sudden stratospheric warming in January 2009, *J. Atmos. Sci.*, 77, 3321 – 3342, <https://doi.org/10.1175/JAS-D-20-0039.1>, 2020.
- Strube, C., Ern, M., Preusse, P., and Riese, M.: Removing spurious inertial instability signals from gravity wave temperature perturbations using spectral filtering methods, *Atmos. Meas. Tech.*, 13, 4927–4945, <https://doi.org/10.5194/amt-13-4927-2020>, 2020.
- 1225 Strube, C., Preusse, P., Ern, M., and Riese, M.: Propagation Paths and Source Distributions of Resolved Gravity Waves in ECMWF-IFS analysis fields around the Southern Polar Night Jet, *Atmos. Chem. Phys.*, 21, 18 641–18 668, <https://doi.org/10.5194/acp-21-18641-2021>, 2021.
- Taylor, M. J., Ryan, E. H., Tuan, T. F., and Edwards, R.: Evidence of preferential directions for gravity wave propagation due to wind filtering in the middle atmosphere, *J. Geophys. Res.*, 98, 6047–6057, <https://doi.org/10.1029/92JA02604>, 1993.
- 1230 Thayer, J. P., Rapp, M., Gerrard, A. J., Gudmundsson, E., and Kane, T. J.: Gravity-wave influences on Arctic mesospheric clouds as determined by a Rayleigh lidar at Sondrestrom, Greenland, *Journal of Geophysical Research: Atmospheres*, 108, <https://doi.org/https://doi.org/10.1029/2002JD002363>, 2003.
- Trinh, Q. T., Kalisch, S., Preusse, P., Chun, H.-Y., Eckermann, S. D., Ern, M., and Riese, M.: A comprehensive observational filter for satellite infrared limb sounding of gravity waves, *Atmos. Meas. Tech.*, 8, 1491–1517, <https://doi.org/10.5194/amt-8-1491-2015>, 2015.
- 1235 Trinh, Q. T., Kalisch, S., Preusse, P., Ern, M., Chun, H.-Y., Eckermann, S. D., Kang, M.-J., and Riese, M.: Tuning of a convective gravity wave source scheme based on HIRDLS observations, *Atmos. Chem. Phys.*, 16, 7335–7356, <https://doi.org/10.5194/acp-16-7335-2016>, 2016.
- Watanabe, S., Sato, K., and Takahashi, M.: A general circulation model study of the orographic gravity waves over Antarctica excited by katabatic winds, *J. Geophys. Res.*, 111, <https://doi.org/10.1029/2005JD006851>, 2006.
- 1240

- Whiteway, A. J., Duck, T. J., Donovan, D. P., Bird, J. C., Pal, S. R., and Carswell, A. I.: Measurements of gravity wave activity within and around the arctic stratospheric vortex, *Geophys. Res. Lett.*, 24, 1387–1390, 1997.
- Williams, P. D., Read, P. L., and Haine, T. W. N.: Spontaneous generation and impact of inertia-gravity waves in a stratified, two-layer shear flow, *Geophysical Research Letters*, 30, <https://doi.org/https://doi.org/10.1029/2003GL018498>, 2003.
- 1245 Worthington, R. M.: Mountain waves launched by convective activity within the boundary layer above mountains, 103, 469–491, <https://doi.org/10.1023/A:1014965029602>, 2002.
- Worthington, R. M.: Organisation of orographic convection by mountain waves above Cross Fell and Wales, 70, 186–188, <https://doi.org/10.1002/wea.2475>, 2015.
- Wright, C. J., Osprey, S. M., Barnett, J. J., Gray, L. J., and Gille, J. C.: High Resolution Dynamics Limb Sounder measurements of gravity wave activity in the 2006 Arctic stratosphere, *J. Geophys. Res.*, <https://doi.org/10.1029/2009JD011858>, 2009.
- 1250 Wright, C. J., Hindley, N. P., Alexander, M. J., Barlow, M., Hoffmann, L., Mitchell, C. N., Prata, F., Bouillon, M., Carstens, J., Clerbaux, C., Osprey, S. M., Powell, N., Randall, C. E., and Yue, J.: Surface-to-space atmospheric waves from Hunga Tonga-Hunga Ha’apai eruption, *Nature*, p. prerelease, <https://doi.org/https://doi.org/10.1038/s41586-022-05012-5>, 2022.
- Wu, D. L. and Eckermann, S. D.: Global Gravity Wave Variances from Aura MLS: Characteristics and Interpretation, *J. Atmos. Sci.*, 65, 3695–3718, <https://doi.org/10.1175/2008JAS2489.1>, 2008.
- 1255 Xie, J., Zhang, M., Xie, Z., Liu, H., Chai, Z., He, J., and Zhang, H.: An Orographic-Drag Parametrization Scheme Including Orographic Anisotropy for All Flow Directions, *Journal of Advances in Modeling Earth Systems*, 12, <https://doi.org/10.1029/2019MS001921>, 2020.
- Yan, X., Arnold, N., and Remedios, J.: Global observations of gravity waves from High Resolution Dynamics Limb Sounder temperature measurements: A yearlong record of temperature amplitude and vertical wavelength, *J. Geophys. Res. Atmos.*, 115, D10 113, <https://doi.org/10.1029/2008JD011511>, 2010.
- 1260 Zhu, X.: Radiative damping revisited - Parametrization of damping rate in the middle atmosphere, *J. Atmos. Sci.*, 50, 3008–3021, [https://doi.org/10.1175/1520-0469\(1993\)050<3008:RDRPOD>2.0.CO;2](https://doi.org/10.1175/1520-0469(1993)050<3008:RDRPOD>2.0.CO;2), 1993.

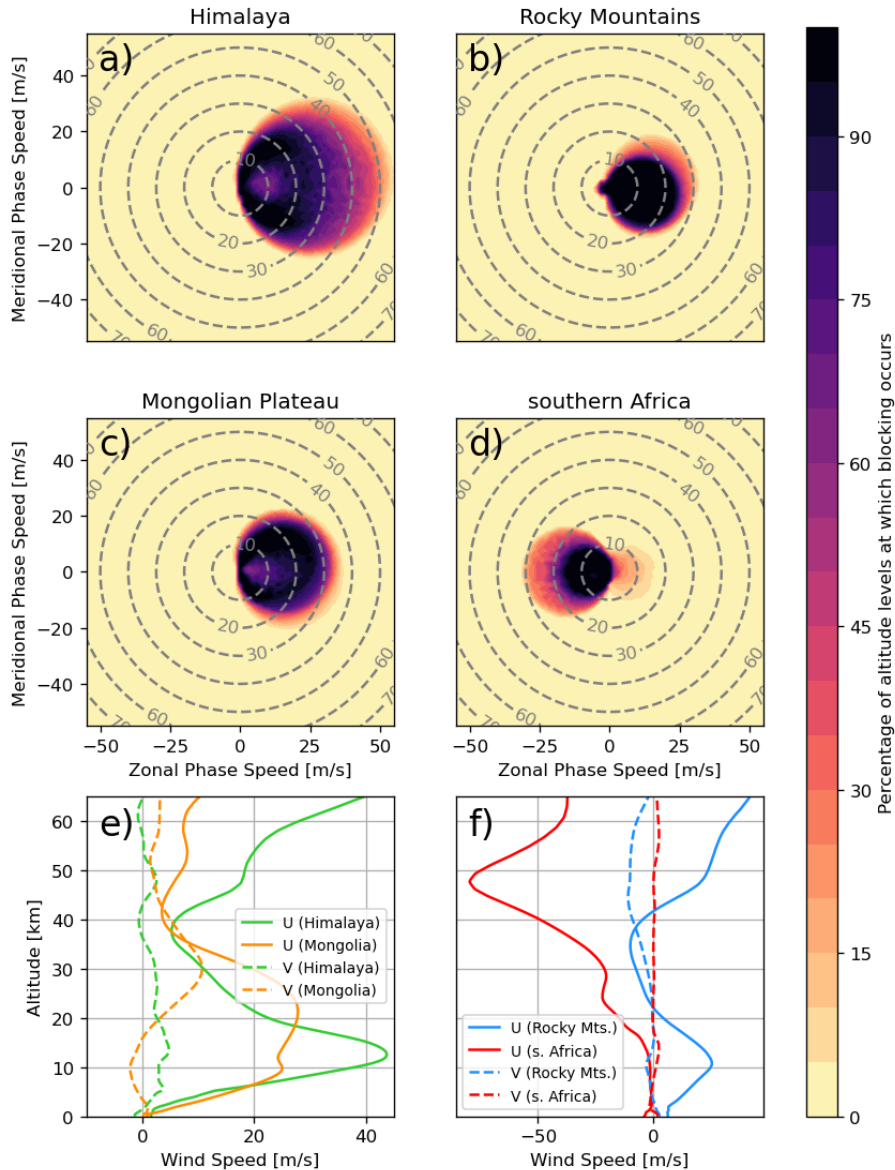


Figure 9. Blocking diagrams as introduced in Taylor et al. (1993) for the four regions shown in Fig. 8 for the time period of January 2006: a) Himalaya, b) Brazil, c) Mongolian plateau and d) southern Africa. **Percentage-Color shading gives the fraction of altitude levels at which blocking occurs of between the surface and 25 km that exhibit a gravity wave with critical level for the corresponding part of the GW phase speed given on the axes is shown in color shading spectrum. These percentages are calculated. Alternatively this can be interpreted as an estimate on the probability that a mean over all vertical wind profiles-GW of the regions from surface to given (ground-based) phase speed passes beyond 25 km altitude without being filtered by a critical level. The mean wind profile of the considered region has been taken for the calculation of blocking occurring at each individual level.** Panels e) and f) show the monthly mean vertical profiles of zonal (solid) and meridional (dashed) wind for the Himalaya and Mongolian Plateau regions and Brazil and southern Africa region, respectively (colors correspond to the regions in Fig. 8).

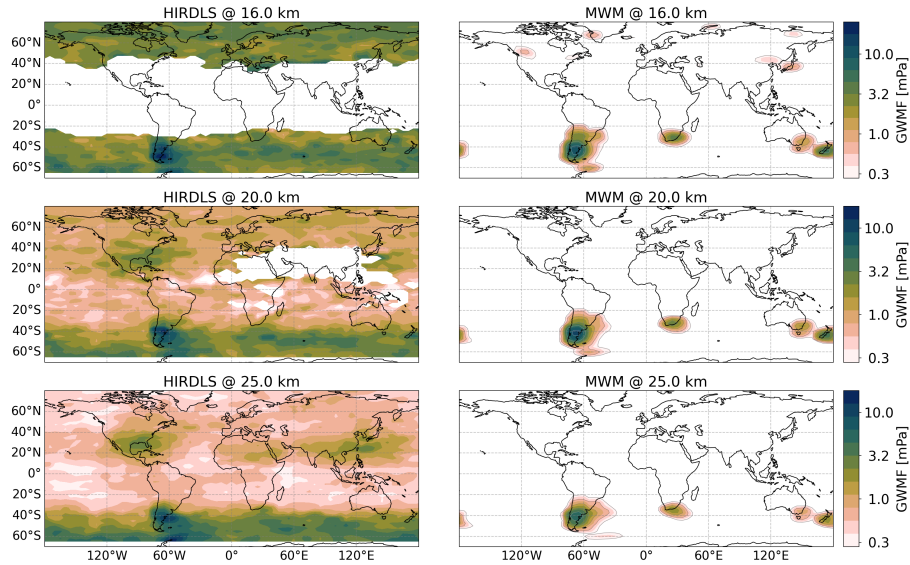


Figure 10. Same as Fig. 6 but for July 2006. Note the logarithmic color scales.

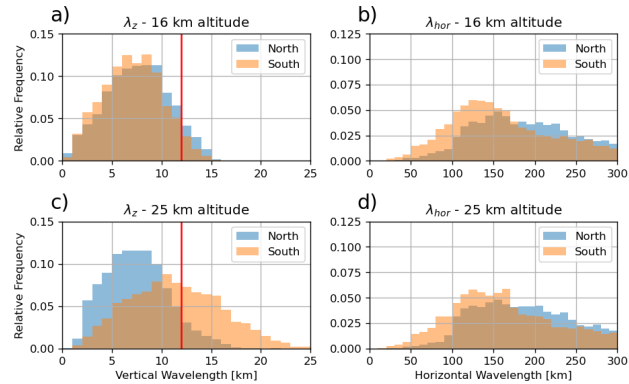


Figure 11. Distribution of vertical (left) and horizontal (right) wavelengths as found by the MWM at altitudes of 16 km (top) and 25 km (bottom). The northern region corresponds to 37° - 47° S and the southern region to 47° - 57° S, both between 40° - 90° W. The vertical red line in panels a) and c) marks the cutoff wavelength of $\lambda_z = 12$ km for the present HIRDLS data.

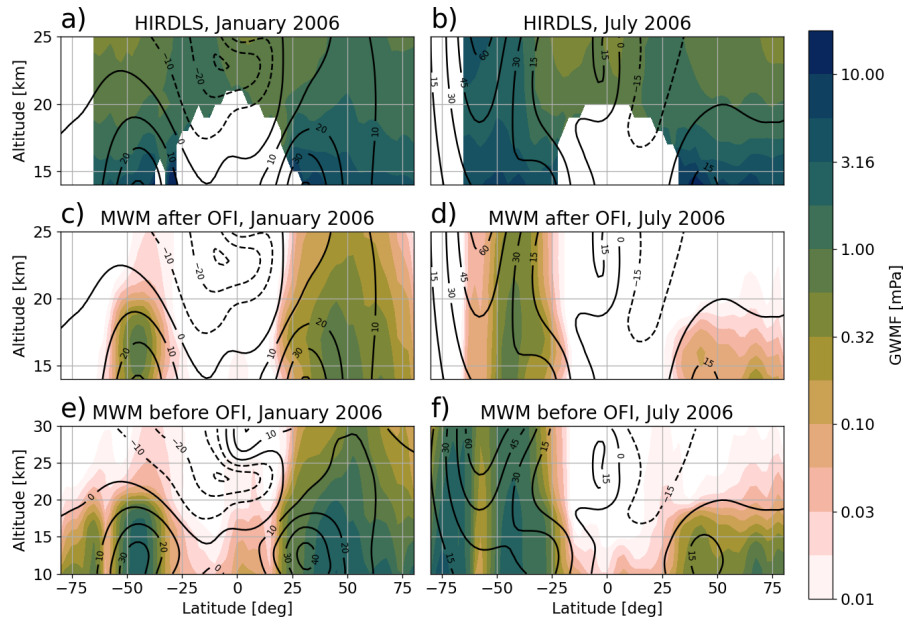


Figure 12. Monthly and zonal mean GWMF for January (left column) and July (right column) 2006. Panels a) and b) show HIRDLS data, panels c) and d) MWM data after application of the observational filter and panels e) and f) MWM data without any filtering. Contour lines show the monthly and zonal mean zonal wind for the corresponding month. Note that panels e) and f) show a wider altitude range than a – d).

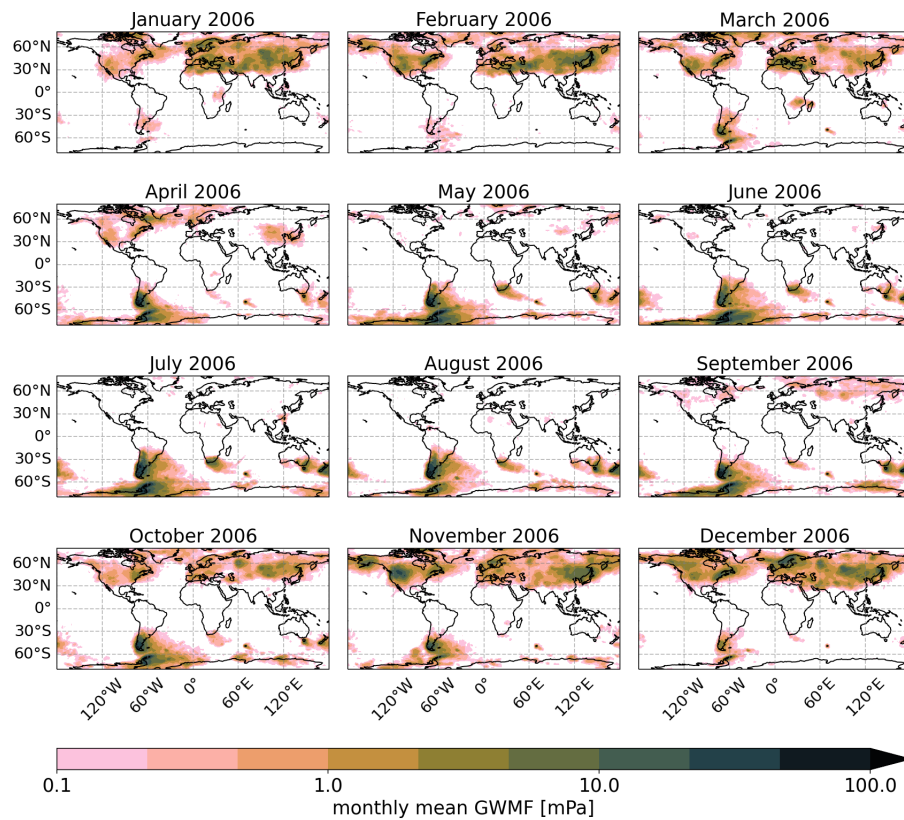


Figure 13. Horizontal monthly mean GWMF distribution for each month of 2006 at 25 km altitude. Shown is MWM data without the observational filter applied.

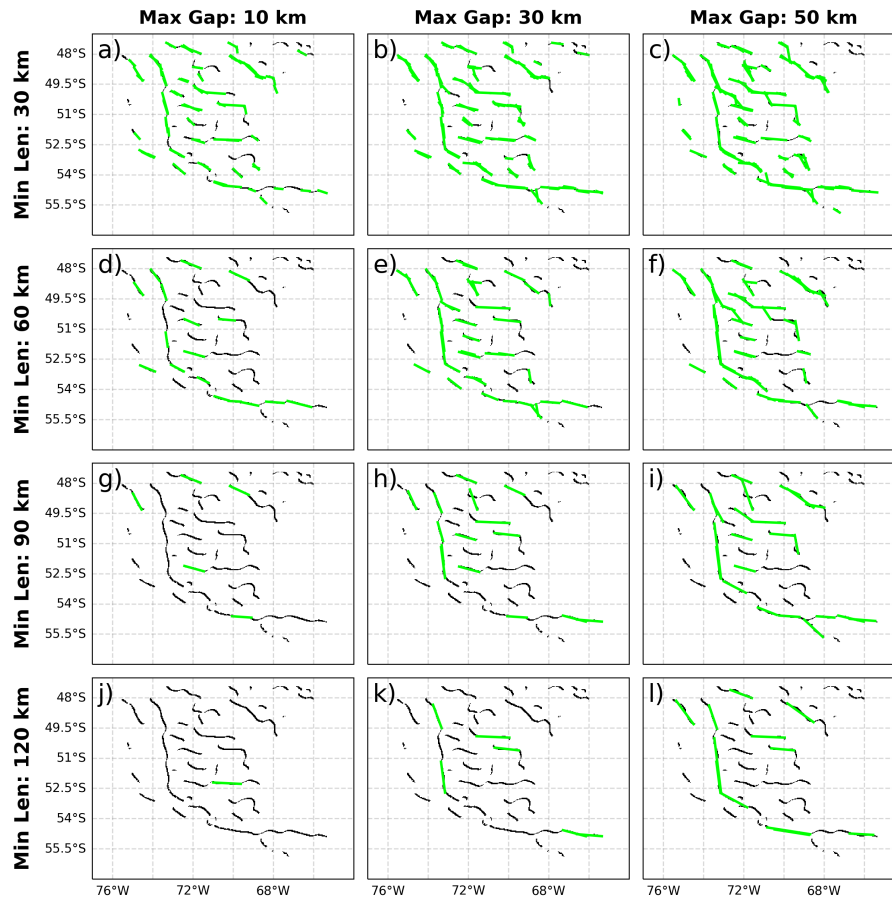


Figure B1. Line structure skeleton of the Southern Andes region after applying a bandpass of scales 100-250/100-200 km. Panel a) shows the underlying structure that is the input to The detected line segments are shown in green on top of the probabilistic Hough transform skeleton. Panel b)–f) show the detected lines (magenta) for different sets Maximum line gap varies from left to right with values of (l_{min}, l_{gap}) : b)–(50/10 km, 20/30 km), e)–(60 and 50 km , 20 in the given column. Minimum line length varies with row with values of 30 km), d)–(60 km, 40 km), e)–(100 km, 30/90 km) and f)–(100/120 km respectively. Panel e shows the parameters, 50 km) that have been used throughout this study.

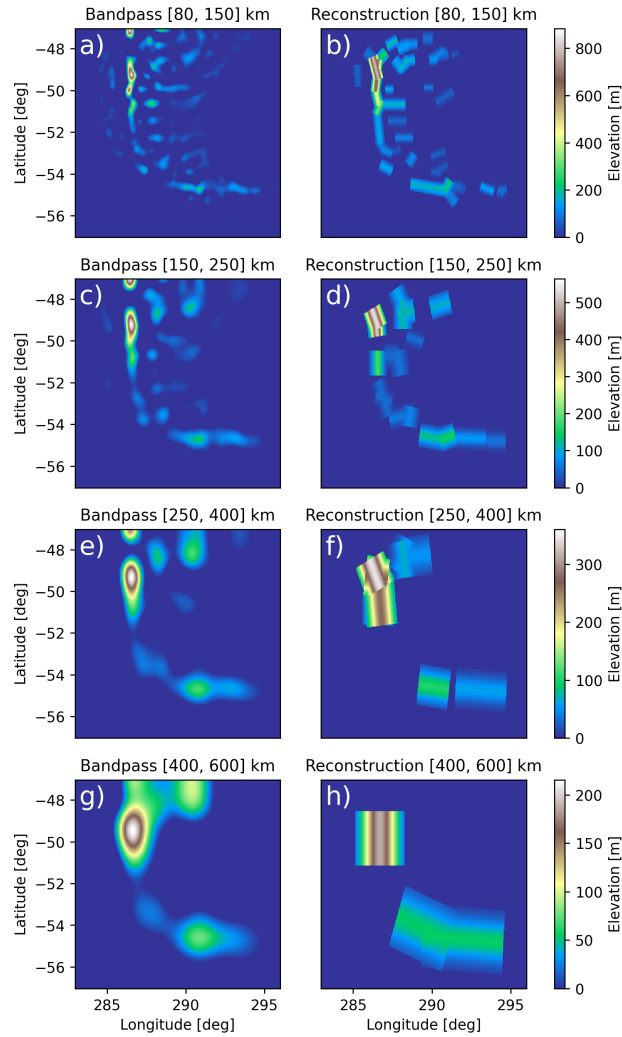


Figure C1. Reconstruction from the different detected idealized two-dimensional ridges in the given bandpass filtered elevation data. The left column show the result of the bandpass filter, the right column the corresponding detected ridges. The spectral band varies with row from smallest to largest scales. For the reconstruction, if multiple ridges cover the same spot, the maximum height was taken. Note that only the four smallest scale intervals yielded ridges and are therefore shown here.

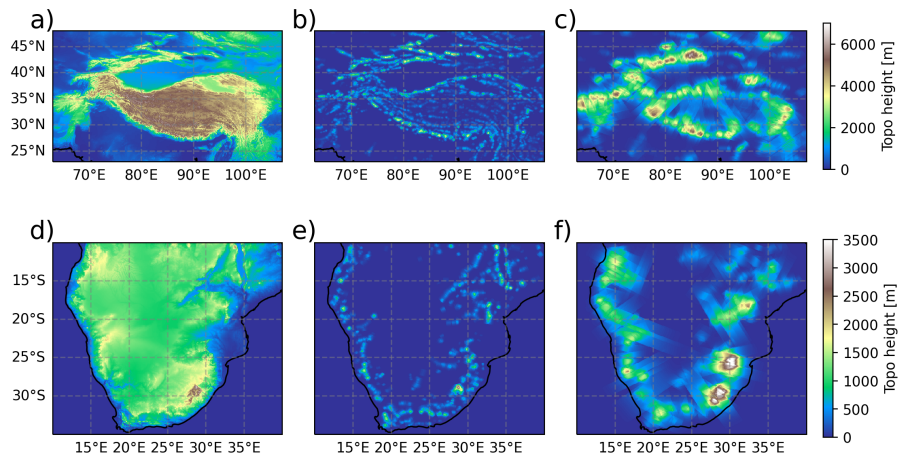


Figure C2. Same as Fig. 2 but for the Mongolia region (a – c) and southern Africa (d – f). The underlying topographic data is shown in panels a and d, respectively, while the reconstruction from the identified idealized Gaussian mountain ridges are shown in panels b, c, e and f. The reconstruction is separated into small scales (≤ 150 km, panels b and e) and large scales (>150 km, panels c and f).

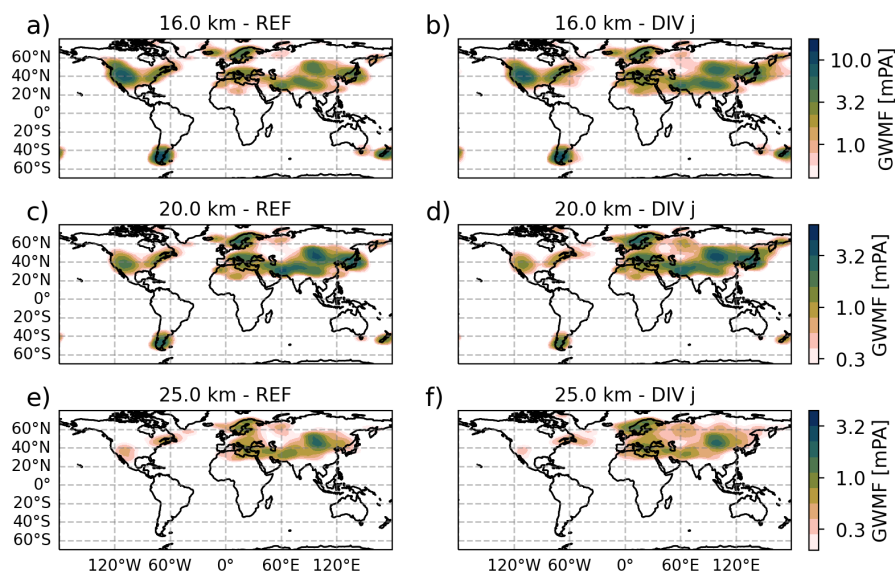


Figure D1. Mountain ridges shown in a similar fashion as in previous studies for the Rocky Mountain region. Similar to Fig. 6, width of the boxes is given by half the wavelength of excited waves, length is given by the length of monthly mean GWMF prediction for January 2006 from the underlying ridge. MWM is shown at different altitudes. Boxes have been drawn in order of ascending height so that the left column uses the highest ridges (which are typically standard GROGRAT amplitude correction, the smaller ones) are visible at top right column a modified version, where the large-scale small amplitude features last term in Eq. 6 is the height approximated locally according to Eq. D1. The observational filter of HIRDLS has been applied to both data sets. Note the single ridge, not the accumulative height of all ridges at that position. logarithmic color scale.

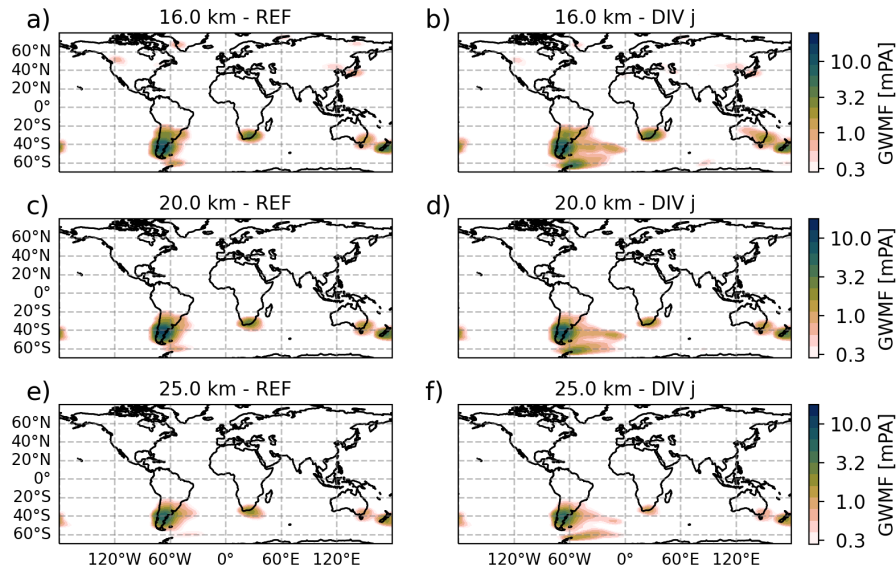


Figure D2. Same as ~~Similar to Fig. ?? but~~ 10, the monthly mean GWMF prediction for July 2006 from the ~~Southern Andes region, which~~ MWM is ~~considered extensively~~ shown at different altitudes. The left column uses the standard GROGRAT amplitude correction, the right column a modified version, where the last term in ~~this study~~ Eq. 6 is approximated locally according to Eq. D1. The observational filter of HIRDLS has been applied to both data sets. Note the logarithmic color scale.